Insights into enhancement of NH_3-SCR activity and N_2 selectivity of LDHs-derived $NiMnAlO_x$ catalysts: Combination of experiments and DFT calculations

Qinghua Yan [a],[1], Jiewen Xiao [b],[1], Rongrong Gui [b], Zhenyu Chen [a], Yuxin Wang [a], Yuran Li [c], Tingyu Zhu [c], Qiang Wang [b],[*], Yanjun Xin [a],[**]

[a] *Qingdao Engineering Research Center for Rural Environment, College of Resources and Environment, Qingdao Agricultural University, Qingdao 266109, PR China*
[b] *College of Environmental Science and Engineering, Beijing Forestry University, 35 Qinghua East Road, Haidian District, Beijing 100083, PR China*
[c] *Research Center for Process Pollution Control, National Engineering Laboratory for Hydrometallurgical Cleaner Production Technology, Institute of Process Engineering, Chinese Academy of Sciences, Beijing 100190, China*

ARTICLE INFO

ABSTRACT

The LDHs-derived $NiMnAlO_x$ catalysts was proposed for NH_3-SCR denitration technology, which improved the overall catalytic performance. At 100–250 ^oC, the preferred $Ni_1Mn_{0.5}Al_{0.5}O_x$ had NO_x conversion of exceeded 95%, and N_2 selectivity of more than 89%, which was higher than the control catalysts. Additionally, $Ni_1Mn_{0.5}Al_{0.5}O_x$ also performed better resistance to SO_2 with less sulfate species deposited on the surface. Transient reaction was conducted to illustrate that $Ni_1Mn_{0.5}Al_{0.5}O_x$ reduced the N_2O formation by suppressing the occurrence of non-selective catalytic pathway. Physicochemical characterization analyses confirmed that $Ni_1Mn_{0.5}Al_{0.5}O_x$ catalyst had more active species, abundant surface oxygen, moderate acidic sites and redox properties, which promoted the adsorption and activation of NO_x and NH_3, and further accelerated the SCR reaction. Finally, DFT calculations provided insights into the mechanism and influence of the degradation of the Jahn-Teller effect and the reversal of the magnetic moment at the Mn site on the surface adsorption process.

1. Introduction

Nitrogen oxides (NO_x) are one of the major pollutants emitted from industrial production, and their harmful effects on the ecosystem and human health cannot be ignored [1,2]. Compared with the existing commercial catalytic systems (V_2O_5-WO_3(MoO_3)/TiO_2) that suffer from decreased N_2 selectivity at high temperatures (573–673 K), high toxicity of V_2O_5, high conversion rate of SO_2 to SO_3, and the need to reheat stack gases [3], the low-temperature selective catalytic reduction (LT-SCR) of NO_x technology has been favored by both scholars and industries. Therefore, from the perspective of energy crisis and global climate deterioration, excellent LT-SCR denitration catalysts are more suitable for practical applications.

In the past decades, large amount of catalysts have been developed for LT-SCR, such as Ce-[4–7], Cu-[8], Fe-[6,9,10], Mn-[11,12] based catalysts. Especially, Mn-based catalysts, possessing a various unstable valence states and remarkable redox properties, have been the hotspot for LT-SCR of NO_x. Although LT-SCR has been studied quite intensively, most of the studies have focused mainly on the conversion of NO, with little attention paid to the conversion of N_2O. The amount of N_2O produced by V_2O_5 based catalysts is usually small, but considerable formation of N_2O has been detected in SCR processes using Mn-based catalysts at low temperature. For SCR technology, N_2O from NO conversion is another form of pollution and due to its high stability, it is more effective than CO_2 and CH_4 in causing stratospheric ozone depletion. In addition, it has been shown that the high performance of catalysts even at high temperatures above 300 ^oC may be attributed to the decomposition of N_2O. Therefore, exploring the pathway and mechanism of N_2O generation is crucial for the development of Mn-based catalysts with overall excellent performance.

Generally, N_2O can generate from the direct oxidation of NH_3 [13, 14], the non-selective catalytic reaction [15,16], and the NO

disproportionation reaction [16]. Ren et al. [17] found that the N_2O accumulation on the $MnFeO_x$ catalyst at low temperature ($<150\ ^oC$) mainly came from the non-selective catalytic reaction pathway, and then gradually shifted to NH_3 over-oxidation with the increase of temperature. Moreover, NH_2NO and NH_4NO_2 intermediates played a vital part in NH_3-SCR reaction and prevented the generation of N_2O [18]. Metal element doping modification is undoubtedly an efficient strategy for improving the overall performance of Mn-based SCR catalysis [19, 20]. Chen et al. [21] reported that the synergistic effect of Ni and Mn formed by electron transfer can improve the redox ability of the Mn-based catalyst, thereby promoting the DeNO$_x$ activity and N_2 selectivity. The contribution value of the above reaction path for the formation of N_2O, and the essential change process of reaction molecules for Mn-based catalysts were not yet very clear. Wan et al. [22] reported that the preferred Ni(0.4)-MnO$_x$ catalyst reached nearly 100% NO$_x$ conversion in the NH_3-SCR of NO$_x$ at 150–240 ^oC, and possessed certain resistance to SO_2. However, its N_2 selectivity was still unsatisfactory, only 70% at low temperatures. Deng et al. [23] confirmed that the introduction of Fe can improve the overall performance of Fe (0.5)-MnO$_x$/TiO$_2$ catalyst, but its activity at low temperatures and N_2 selectivity at high temperatures still need to be improved. For LT-SCR catalysts, the dispersion state of MnO$_x$ is one of the decisive factors for catalytic activity [23]. Smirniotis et al. [24] reported that the aggregate state of MnO$_x$ has a great influence on the performance of the catalyst. Kijlstra et al. [25] also proposed that the aggregated MnO$_x$ phase can accelerate the production of N_2O, which affected the N_2 selectivity. Therefore, the high dispersion state of the active component is the non-negligible parameter for designing an excellent LT-SCR catalyst.

However, the conventional catalyst preparation methods (e.g., impregnation and co-precipitation) lead to poor dispersion of the highly loaded amorphous Mn phase, which reduces denitrification activity [16]. Recently, SCR catalysts produced by the layered double hydroxides (LDHs) derived catalyst method have shown excellent catalytic activity, lower apparent activity energy, and better dispersion of active particles compared to most of the previously reported SCR catalysts. LDHs are a class of two-dimensional nanostructured layered anionic materials, and its laminated metal cations and interlayer anions have adjustable properties [26,27]. The LDHs material can be calcined at high temperature to obtain layered double oxides (LDOs) with large specific surface area, high dispersion of active components and controllability, which has become the potential application material in various fields, such as CO_2 capture [28,29], adsorbents [30,31], catalysts [32,33], and two-dimensional membrane materials [34].

Herein, we designed the LDHs-derived $NiMnAlO_x$ mixed oxides, which may be excellent NH_3-SCR catalysts for NO_x, especially for low-temperature activity and N_2 selectivity. The high dispersibility and controllability of LDHs-derived oxides, as well as the advantage of Ni element, were fully combined to broaden the catalytic temperature window and improve N_2 selectivity and resistance to SO_2. The effects of parameters such as metal composition and calcination conditions on the crystal structure, active species, redox properties, surface acidity and catalytic performance were systematically studied, and the optimal preparation process was clarified. Importantly, the transient reaction was conducted to detect the contribution of the N_2O generation pathways and explain the nature of the excellent N_2 selectivity on the $NiMnAlO_x$-LDO catalysts. Density functional theory (DFT) was combined with in-situ DRIFTS analysis to analyze the electronic layer structure and intermolecular forces, which revealed the adsorption and activation properties of NO_x and NH_3 on the Ni doped Mn-based catalysts, inhibited the overoxidation of NH_3 species, and avoided the further dehydrogenation of NH_2 species, thus increasing the N_2 production.

2. Experimental

2.1. Catalyst preparation

$Ni_yMn_zAl_{1-z}$-CO$_3$ LDHs ($0 < y < 3$, $0 < z < 1$) were prepared by the co-precipitation method. The following will take the preparation of $Ni_1Mn_{0.5}Al_{0.5}$-CO$_3$ LDH as an example: According to a certain ratio, 3.63 g Ni(NO$_3$)$_2$·6 H$_2$O, 1.45 mL 50% Mn(NO$_3$)$_2$, and 2.34 g Al(NO$_3$)$_2$·9 H$_2$O were mixed and configured into a 100 mL solution, add it dropwise to the continuously stirring 100 mL Na$_2$CO$_3$ (0.025 mol) solution, and keep the pH of the system at about 10 by adding 4 M NaOH solution. The temperature during the synthesis was maintained at 60 ^oC and performed under exposure with air. After dripping, keep stirring for 12 h. Then, suction filtration and washing until pH= 7, and stirring the slurry in ethanol solution for 2 h. Finally, it was dried at 60 ^oC and ground for use, and $Ni_1Mn_{0.5}Al_{0.5}$-CO$_3$ LDH was obtained. $Ni_yMn_zAl_{1-z}O_x$ LDOs were obtained by calcination of LDHs at high temperature. In order to systematically evaluate the performance of $Ni_yMn_zAl_{1-z}O_x$, 2 wt% Mn/γ-Al$_2$O$_3$ and 1 wt% Ni-1 wt% Mn/γ-Al$_2$O$_3$ as control catalysts were obtained by the conventional impregnation method [32].

2.2. Catalyst characterization

X-Ray Diffraction (XRD-7000, Shimadzu), Field Emission Scanning Electron Microscope (FE-SEM, SU-8010, Hitachi), and High Resolution Transmission Electron Microscopy (HR-TEM, FEI Tecnai G2 F20, USA) were used to reveal the structural and morphological characteristics of the prepared material. The specific surface area of prepared material was analyzed by N$_2$ sorption/desorption analysis (SSA-7000, Builder). X-ray photoelectron spectroscopy (XPS) analyses was implemented on Thermo Scientific Escalab 250Xi with monochromatic Al kα radiation (hν = 1486.6 eV). The total Mn content in the sample was analyzed by inductively coupled plasma mass spectrometer (ICP-MS, Agilent 7900, USA). Multifunction chemisorption analyzer was used on Builder PCA-1200 to implement SO$_2$/NH$_3$/NO-temparature programmed desorption (SO$_2$/NH$_3$/NO-TPD) and H$_2$-temperature programmed reduction (H$_2$-TPR) analyses. In-situ DRIFT analyses were achieved with the reaction cell (ZnSe window) and diffuser attachment (HARRICK) on Bruker Vertex 70 instrument.

2.3. Catalytic activity measurements

The denitration performance was implemented in a stainless steel reactor with a fixed bed containing about 150 mg of catalyst at a flow rate of 200 mL/min. Equal concentrations (500 ppm) of NO$_x$ and NH$_3$, 5% O$_2$, 5% H$_2$O (if needed) and 100 ppm SO$_2$ (if needed), and the carrier gas Ar together formed the simulation gas. The MultiGas 2000 FTIR Gas Analyzer was selected to monitor the concentrations on-line for 1 h. The corresponding calculation in steady state was done using Eqs. (1)–(3).

$$NO_x\ \text{conversion} = \left(1 - \frac{NO_x(out)}{NO_x(in)}\right) \times 100\% \tag{1}$$

$$N_2\ \text{selectivity} = \left(1 - \frac{2N_2O(out)}{NO_x(in) + NH_3(in) - NO_x(out) - NH_3(out)}\right) \times 100\% \tag{2}$$

$$NH_3\ \text{conversion} = \left(1 - \frac{NH_3(out)}{NH_3(in)}\right) \times 100\% \tag{3}$$

The reaction rate constant (k) can be expressed as a function of the NO$_x$ conversion (%) at different reaction temperatures, using Eq. (4). The NH$_3$-SCR catalytic reaction of NO$_x$ on the catalyst surface follows Arrhenius Eq. (5):

$$k = -\frac{V}{W} \times \ln\left(1 - x\right) \tag{4}$$

$$Lnk = LnA - \frac{Ea}{RT} \quad (5)$$

Here, k (mL•g^{-1}•s^{-1}) represents the reaction rate constant of NH$_3$-SCR reaction, V (mL•s^{-1}) represents the gas flow rate of the reaction, W (g) represents the weight, x represents the NO$_x$ conversion (%) at different reaction temperatures, A represents the pre-exponential factor, Ea represents the apparent activation energy (kJ•mol^{-1}), R represents the gas constant, T represents the thermodynamic temperature (K). The reaction order of the NH$_3$-SCR reaction of NO$_x$ is close to the first order for NO and the zero order for NH$_3$.

2.4. Transient reaction and NO + O$_2$ reaction

The transient reaction was implemented at 250 °C, the amount of catalyst was 0.15 g, the total gas flow rate was 200 mL/min, and the transient reaction time of "NH$_3$ +O$_2$" and "NO+O$_2$" was 1 h. The feed gas containing 500 ppm NH$_3$, 5% O$_2$, and Ar as balance gas was firstly introduced into the reactor to simulate the NH$_3$ oxidation reaction [13, 14]. After the reaction reached steady state, another 500 ppm NO$_x$ was introduced into the feed gas to simulate the NH$_3$-SCR reaction, and keeping the concentration of other gases unchanged. The concentration of gas (NH$_3$, NO, NO$_2$ and N$_2$O) was monitored online by MultiGas 2000 analyzer.

The NO + O$_2$ reaction was also implement at 250 °C. A mixed gas containing NO$_x$ (500 ppm), 5% O$_2$ and Ar was introduced into the reactor to simulate the NO disproportionation reaction [16].

2.5. DFT calculations

As the result of characterized by XRD (see Section 3.5), Mn/γ-Al$_2$O$_3$ was modeled by (110) surface of α-MnO$_2$ (JCPDS No.24–0735). Because the characteristic peak of NiO phase appeared rather than Mn species, the NiMnAlO$_x$ catalyst was constructed by NiO phase (JCPDS No. 47–1049). The (111) plane of NiO was observed by HR-TEM (see Section 3.1), so the surface of NiMnAlO$_x$ catalyst was modeled by (111) surface of (2 ×2) NiO. For simulating the Mn active site on NiMnAlO$_x$ catalyst, a central Ni atom on (111) surface of NiO was replaced to Mn. The dispersion was taken into account by constructing the supercell, while the interaction between Mn atoms was taken into account by using the periodicity of the model. For the Ni-Mn/γ-Al$_2$O$_3$ and NiMnAlO$_x$ catalysts have the same catalytic active sites, the Ni-Mn/γ-Al$_2$O$_3$ can be explained at same time. The Lewis acid sites of Mn on the surfaces were selected as the adsorption sites of NO and NH$_3$.

Computational simulations were implemented by Vienna ab-initio simulation package (VASP) with the projector augmented wave pseudo-potentials (PAW) to describe the interaction between atomic cores and valence electrons. The Perdew–Burke–Ernzerhof (PBE) functional within the generalized gradient approximation (GGA) were used to implement density functional theory (DFT) calculations [35]. Eight layered NiO (111) slab models and $5 \times 5 \times 1$ Monkhorst Pack k-point sampling were employed to simulate the NiO surface. Four layered MnO$_2$ (110) slab models with $3 \times 4 \times 1$ Monkhorst Pack k-point sampling were employed to simulate the MnO$_2$ surface. In all of the structure optimization calculations, the bottom two layers were fixed, while the other atoms were fully relaxed. The reasonable vacuum layers were set around 15 Å in the z-directions for avoiding interaction between planes. A cutoff energy of 400 eV was provided was chosen for the well converged energy values. Geometry optimizations were pursued until the force on each atom falls below the convergence criterion of 0.02 eV/Å and energies were converged within 10^{-6} eV. The spin polarized method was applied and the magnetic moments were calculated for all magnetic structures. Ferromagnetic and antiferromagnetic NiO bulk cells were calculated, and the lower energy anti-ferromagnetism was chosen for the magnetic calculations of NiO (111). Ferromagnetism was used in the magnetic calculations for MnO$_2$.

The Hubbard corrections (DFT+U) of Mn and Ni were U$_{eff}$ = 2.8 eV (U = 4.0 eV, J = 1.2 eV) and U$_{eff}$ = 5.0 eV (U = 5.0 eV, J = 0 eV).

The adsorption ability was evaluated using the adsorption energy term (E$_{ads}$), which was calculated as follows:

$$E_{ads} = E_{NO/NH_3 + surface} - \left(E_{surface} + E_{NO/NH_3} \right) \quad (6)$$

E$_{surface}$ represents the material surface energy, E$_{NO/NH_3+surface}$ represents the energy of the surface of the material after absorption of NO or NH$_3$ molecules, and E$_{NO/NH_3}$ represents the energy of isolated NO or NH$_3$ molecule.

The d band center (ε$_d$) [36] of material was evaluated as follows:

$$\varepsilon_d = \frac{\int_{-\infty}^{\infty} n_d(\varepsilon)\varepsilon d\varepsilon}{\int_{-\infty}^{\infty} n_d(\varepsilon)d\varepsilon} \quad (7)$$

where ε is energy and $n_d(\varepsilon)$ is the density of d-state.

The differential charge densities were calculated as follows:

$$\Delta\rho = \rho_{AB} - \rho_A - \rho_B \quad (8)$$

where $\Delta\rho$ is differential charge density, ρ_{AB} is the charge density of system after reaction, the ρ_A is the charge density of the initial state of the system and the ρ_B is the charge density of the final state.

3. Results and discussion

3.1. Structural characterization

Ni$_y$Mn$_z$Al$_{1-z}$-CO$_3$ LDHs were first examined using XRD analyses (Fig. 1a). NiMnAl-CO$_3$ LDHs samples all showed the typical layered structure similar to MgAl hydrotalcite in XRD patterns [37]. The peaks were observed at 2θ = 11.42°, 23.04°, 34.64°, 38.9°, 46.58°, 60.4° and 61.64°, corresponding to the reflections of the (003), (006), (009), (015), (018), (110), and (113) crystal planes, respectively. Fig. S1 showed that Ni$_y$Mn$_z$Al$_{1-z}$-CO$_3$ LDHs were converted to metal oxide mixtures after calcination at 400 °C for 5 h. For Ni$_y$Mn$_z$Al$_{1-z}$O$_x$ LDOs, there are three main diffraction peaks appearing at about 37.25°, 43.28° and 63.2°, which belong to NiO phase (JCPDS No. 47–1049). Compared with MnO$_2$ phase (JCPDS No. 24–0735) as the active component in Mn/γ-Al$_2$O$_3$ catalyst (Fig. 1b), no characteristic peaks of the Mn phase were observed in Ni$_1$Mn$_{0.5}$Al$_{0.5}$O$_x$ and Ni-Mn/γ-Al$_2$O$_3$, but the characteristic peak of NiO phase (JCPDS No. 47–1049) appeared, suggesting that Mn species was highly dispersed after the introduction of Ni species. The morphology of Ni$_1$Mn$_{0.5}$Al$_{0.5}$-CO$_3$ LDH was also detected by FE-SEM (Fig. S2). Ni$_1$Mn$_{0.5}$Al$_{0.5}$-CO$_3$ LDH displayed nanosheet morphology [38]. After calcination at 400 °C for 5 h, the morphology of Ni$_1$Mn$_{0.5}$Al$_{0.5}$O$_x$ LDO remained almost unchanged (Fig. 1c), similar to that of the LDH material, which was also confirmed in the HR-TEM images (Fig. 1d, e). The lattice fringe spacing of ca. 0.204 nm were observed, referring to the NiO (111) plane (Fig. 1f). In addition, TEM-EDS and elemental mapping analysis also confirmed the presence of Mn and Ni species in Ni$_1$Mn$_{0.5}$Al$_{0.5}$O in a highly dispersed state (Fig. 1g, h). There are similar conclusions that the introduction of another metal element can improve the dispersibility of Mn species, thereby improving the performance of the catalyst [12].

3.2. Catalytic performance

The DeNO$_x$ performance of Ni$_y$Mn$_z$Al$_{1-z}$O$_x$ catalysts were investigated in a wide temperature range (100–300 °C). Fig. S3a showed the DeNO$_x$ performance of Ni$_y$Mn$_z$Al$_{1-z}$O$_x$ catalysts increased as reaction temperature increasing from 100 to 200 °C, and then started to decline slowly. In particular, the Ni$_1$Mn$_{0.5}$Al$_{0.5}$O$_x$ catalyst exhibited the superior NH$_3$-SCR activity, especially at low temperatures (100–250 °C) with above 95% NO$_x$ conversion. According to the results of the catalytic activity, if the y value exceeded 1, the NO$_x$ conversion decreased, which
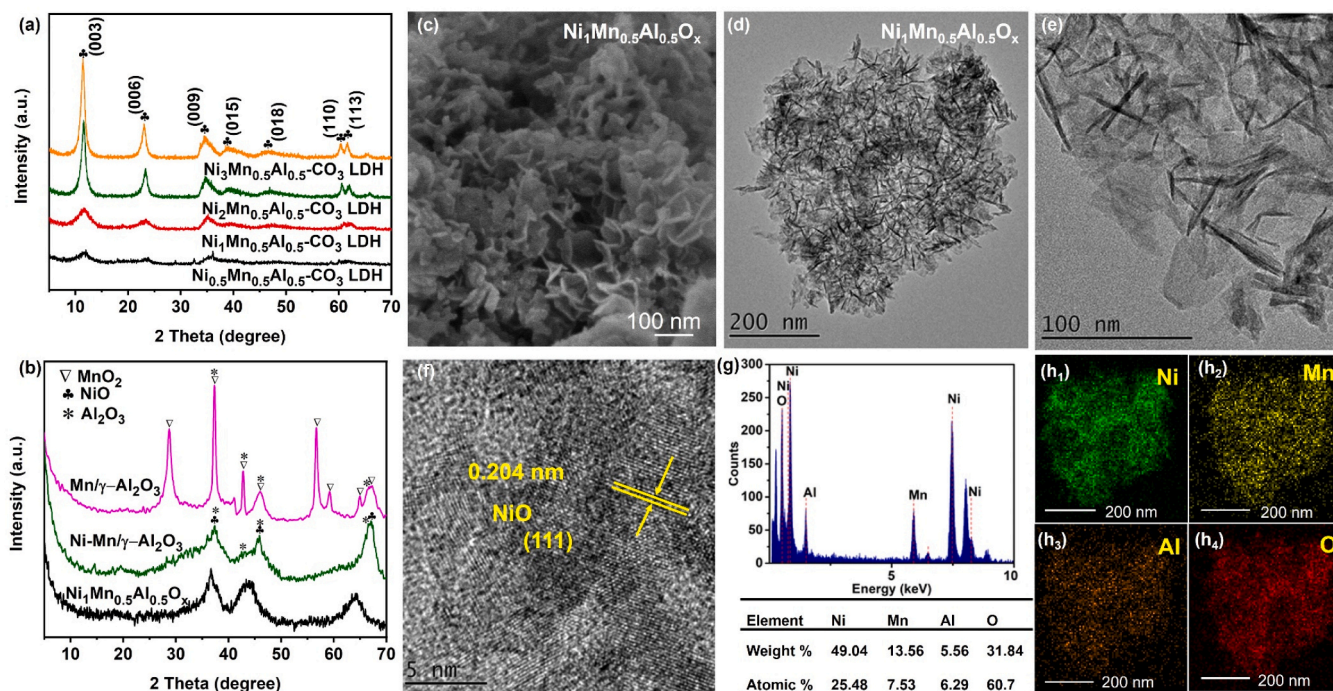
**Fig. 1.** XRD patterns of (a) $Ni_yMn_zAl_{1-z}$-CO_3 LDHs and (b) Mn/γ-Al_2O_3, Ni-Mn/γ-Al_2O_3 and $Ni_1Mn_{0.5}Al_{0.5}O_x$ catalysts, (c) SEM image of $Ni_1Mn_{0.5}Al_{0.5}O_x$ LDO, (d-f) HR-TEM images of $Ni_1Mn_{0.5}Al_{0.5}O_x$, (g) TEM-EDS analysis of $Ni_1Mn_{0.5}Al_{0.5}O_x$ solids, (h) EDS elemental mapping of Ni (h_1), Mn (h_2), Al (h_3) and O (h_4) in $Ni_1Mn_{0.5}Al_{0.5}O_x$.

may be related to the maximum loading of the support [39,40]. Therefore, $Ni_1Mn_{0.5}Al_{0.5}O_x$ catalyst exhibited the best performance at 100–300 °C, with the maximum NO_x conversion of nearly 100% at 200 °C. In contrast, the control Mn/γ-Al_2O_3 and Ni-Mn/γ-Al_2O_3 exhibited poor low temperature activities, and the maximum NO_x conversions were only 72% and 79% at 200 °C, respectively (Fig. 2a). The NH_3 conversion of catalysts was shown in Fig. S3b. At low temperatures, the NH_3 conversion was very similar to that of the corresponding NO_x
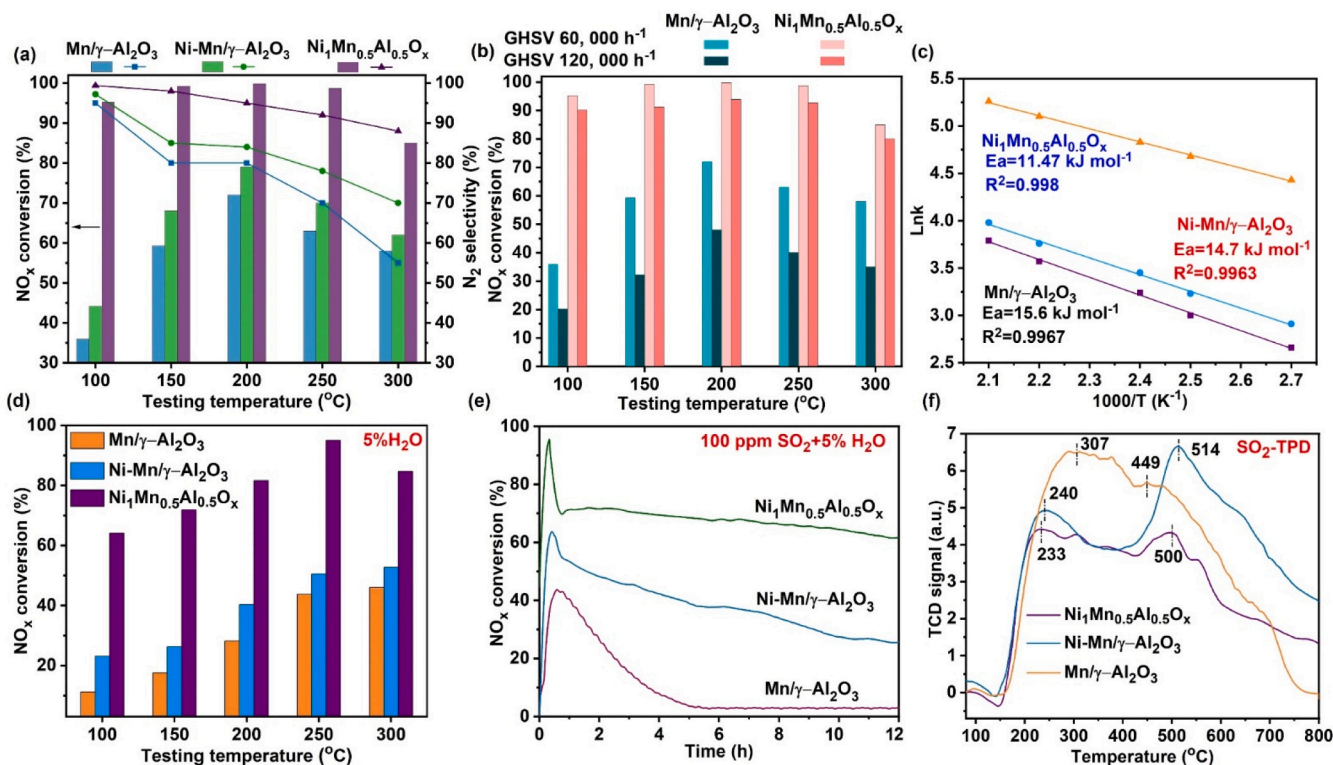
Fig. 2. (a) NO_x conversions and N_2 selectivity, (b) The effect of different GHSVs (GHSV = 60,000 h^{-1}, 120,000 h^{-1}), (c) Arrhenius plots of SCR reaction rates, (d) The effect of 5% H_2O, (e) The effect of 5% H_2O and 100 ppm SO_2 co-existence, (f) SO_2-TPD profiles over Mn/γ-Al_2O_3, Ni-Mn/γ-Al_2O_3 and $Ni_1Mn_{0.5}Al_{0.5}O_x$. Reaction conditions: $[NO_x]$ = $[NH_3]$ = 500 ppm, $[O_2]$ = 5%, balance Ar, total flow rate = 200 mL/min, GHSV = 60,000 h^{-1}, catalyst 0.15 g.

conversion, suggesting that NO and NH_3 almost completely participate in the reaction. The distinct over consumption of NH_3 over $Mn/\gamma\text{-}Al_2O_3$ may be related to the NH_3 oxidation at high temperature (> 250 ^oC). Considering that some unexpected reactions may occurred during the SCR reaction, and one of the main defects of Mn-based catalysts is the poor N_2 selectivity. Fig. 2a showed the N_2 selectivity of $Ni_yMn_zAl_{1-z}O_x$, $Mn/\gamma\text{-}Al_2O_3$, and $Ni\text{-}Mn/\gamma\text{-}Al_2O_3$. It can be seen that $Mn/\gamma\text{-}Al_2O_3$ displayed the lowest N_2 selectivity ($\sim 55\%$) with more N_2O formation, but the N_2 selectivity of $Ni_1Mn_{0.5}Al_{0.5}O_x$ was greatly enhanced to more than 88% at 100–300 ^oC. Therefore, it indicated that both the N_2 selectivity and $DeNO_x$ activity of $Ni_1Mn_{0.5}Al_{0.5}O_x$ could be enhanced by the introduction of Ni. Moreover, $Ni_1Mn_{0.5}Al_{0.5}O_x$ catalyst still exhibited better $DeNO_x$ performance even at higher gas hourly space velocity (GHSV). Increasing the GHSV from 60,000 to 120,000 h^{-1} resulted in only a slight decrease in NO_x conversion for $Ni_1Mn_{0.5}Al_{0.5}O_x$ at the entire test temperature (Fig. 2b). For instance, the NO_x conversion of $Ni_1Mn_{0.5}Al_{0.5}O_x$ slightly decreased from 99.8% to 93% at 200 ^oC. In contrast, the NO_x conversion of $Mn/\gamma\text{-}Al_2O_3$ decreased significantly from 72% to 48% under the same condition. The denitration performance of catalysts after calcination at 350–600 ^oC (Fig. S4). When the calcination temperature was increased from 350 ^oC to 600 ^oC, the $DeNO_x$ performance of $Ni_1Mn_{0.5}Al_{0.5}O_x$ catalyst remained at 89% at 200 ^oC, while $Mn/\gamma\text{-}Al_2O_3$ was only 24.6%. In addition, the optimum catalytic activity of $Ni_1Mn_{0.5}Al_{0.5}O_x$ prepared at a calcination temperature of 400 ^oC reached 99.8%. Therefore, the addition of Ni in combination with the LDHs-derived catalyst approach not only improved $DeNO_x$ activity and N_2 selectivity, but also broadened the operating temperature range of Mn-based catalysts.

As we all know, the reaction rate was closely related to the activation energy (Ea). The lower the activation energy, the better the catalytic activity. The activation energy (Ea) of low-medium temperature NH_3-SCR reaction can be calculated from the slope of linear Lnk and 1000/T. In Fig. 2c, the Arrhenius curves of the three catalysts had a good linear relationship between Lnk and 1000/T. For the $Ni_1Mn_{0.5}Al_{0.5}O_x$, the activation energy (11.47 kJ•mol^{-1}) was lower than that of $Ni\text{-}Mn/\gamma\text{-}Al_2O_3$ (14.7 kJ•mol^{-1}) and $Mn/\gamma\text{-}Al_2O_3$ (15.6 kJ•mol^{-1}). The activation energy (Ea) results further confirmed that the Ni modified $Ni_1Mn_{0.5}Al_{0.5}O_x$ catalyst has higher catalytic activity in LT-SCR reaction.
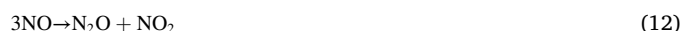
3.3. SO_2 and/or H_2O resistance of catalysts

High resistance to SO_2 and H_2O was quite necessary as they are usually present in the flue gas. SO_2 poisoning was mainly to form $(NH_4)_2SO_4/NH_4HSO_4$ or metal sulfate species, which was even more serious for Mn-based catalysts. The effects of H_2O are mainly attributed to compete with active sites for reactive species (NO_x, NH_3, etc.). Thus, we investigated the effect of SO_2 and/or H_2O on the $DeNO_x$ activity of catalysts. With introducing 5% H_2O, the $DeNO_x$ activity of $Mn/\gamma\text{-}Al_2O_3$ was lower than that of $Ni_1Mn_{0.5}Al_{0.5}O_x$ (95%) and $Ni\text{-}Mn/\gamma\text{-}Al_2O_3$ (50.5%) at 250 ^oC (Fig. 2d). In addition, the optimal reaction temperature of the catalyst shifted toward the high temperature from 200 to 250 ^oC, which indicated that H_2O poisoning on the catalyst at low temperature was lower than that at high temperature. Fig. S5 showed the $DeNO_x$ activity of catalysts decreased after being exposed to 100 ppm SO_2 at 200 ^oC. After 6 h, the $DeNO_x$ activity of $Mn/\gamma\text{-}Al_2O_3$ ($\sim 8.1\%$) was much lower than that of $Ni_1Mn_{0.5}Al_{0.5}O_x$ ($\sim 73\%$) and $Ni\text{-}Mn/\gamma\text{-}Al_2O_3$ ($\sim 45.2\%$).

In practical working conditions, both H_2O and SO_2 coexisted in the flue gases. Thus, the effect of co-existence of 100 ppm SO_2 + 5% H_2O on the $DeNO_x$ activity should be considered, and each experiment was performed for 12 h (Fig. 2e). The $DeNO_x$ activity dropped significantly from 72% to 3.1% ($Mn/\gamma\text{-}Al_2O_3$) and 79–25.6% ($Ni\text{-}Mn/\gamma\text{-}Al_2O_3$) at 200 ^oC, respectively. However, under the same condition, $Ni_1Mn_{0.5}Al_{0.5}O_x$ still achieved 61.7% NO_x conversion. SO_2-TPD experiments were implemented on catalysts (Fig. 2f). Two desorption peaks were obtained for all catalysts in the ranges of 235–337 ^oC and 448–507 ^oC, which

were the decomposition of $(NH_4)_2SO_4/NH_4HSO_4$ and metal sulfate species, respectively. From the peak area of the desorption peak, $Mn/\gamma\text{-}Al_2O_3$ had more sulfate species deposited, so it was more susceptible to SO_2, while $Ni_1Mn_{0.5}Al_{0.5}O_x$ catalyst had less sulfate formation, and the negative effect of SO_2 on the $DeNO_x$ activity was weakened. Therefore, it was evident that the doping of Ni can alleviate the effect of H_2O and/or SO_2 poisoning and improve the stability of the catalyst.

3.4. Transient kinetics studies for the formation of N_2O

N_2O and N_2 are often simultaneously formed in the NH_3-SCR reaction of NO_x. N_2O may be formed by the following four reactions (Eqs. (9)–(12)):

$$2NH_3 + 2O_2 \rightarrow N_2O + 3H_2O \tag{9}$$

$$4NO + 4NH_3 + 3O_2 \rightarrow 4N_2O + 6H_2O \tag{10}$$

$$4NO_2 + 4NH_3 + O_2 \rightarrow 4N_2O + 6H_2O \tag{11}$$

$$3NO \rightarrow N_2O + NO_2 \tag{12}$$

In the NH_3-SCR process, the NH_3 oxidation (Eq. (9)) was considered to be the main source of N_2O formation [13]. Therefore, we investigated the catalytic performance of catalysts for the "$NH_3 + O_2$" reaction. In Fig. 3a, the conversion of NH_3 became higher as the temperature increases. At 300 ^oC, the NH_3 conversion of $Mn/\gamma\text{-}Al_2O_3$ was 30%, which was slightly higher than $Ni\text{-}Mn/\gamma\text{-}Al_2O_3$ (28%) and $Ni_1Mn_{0.5}Al_{0.5}O_x$ (26.8%). More importantly, with the introduction of Ni, the formation of N_2O can be reduced, especially at low temperatures. The amount of N_2O produced by the "$NH_3 + O_2$" reaction and the SCR reaction were also compared in this work. For $Ni_1Mn_{0.5}Al_{0.5}O_x$ catalyst, the amount of N_2O produced by the two reactions was almost equal (T $= 250$ ^oC, ~ 50 ppm N_2O). For $Ni\text{-}Mn/\gamma\text{-}Al_2O_3$ and $Mn/\gamma\text{-}Al_2O_3$, the amounts of N_2O produced by "$NH_3 + O_2$" reaction were much lower than the that by SCR reaction, which were 60.2 ppm, 67 ppm for "$NH_3 + O_2$" reaction, and 82 ppm, 101 ppm for SCR reaction, respectively (Fig. 3a, b). Obviously, for the $Ni_1Mn_{0.5}Al_{0.5}O_x$ catalyst, N_2O was mainly generated by "$NH_3 + O_2$" reaction, while the control catalysts have other pathways to produce N_2O.

In order to further study other reaction pathways, we performed transient reaction studies on the above three samples. After the "$NH_3 + O_2$" reaction reached a steady state, 500 ppm NO_x was introduced in the flue stream, and the concentration changes of each component (N_2O, NO, and NO_2) were monitored. Fig. 3c displayed that the N_2O concentration of the control catalysts increased significantly, while $Ni_1Mn_{0.5}Al_{0.5}O_x$ was only slightly increased. Therefore, the non-selective catalytic "$NH_3 + O_2 + NO_x$" reaction (Eqs. (10−11)) also contributed to the formation of N_2O for the control catalysts, which was consistent with the conclusions of previous reports [13]. In addition, we also carried out NO oxidation reaction, as shown in Fig. 3d. There was nearly no N_2O generation (~ 2.3 ppm N_2O) for the three samples, indicating that N_2O generation can ignore the NO_x disproportionation reaction (Eq. (12)). For the control catalysts, "$NH_3 + O_2$" and non-selective catalytic "$NH_3 + O_2 + NO_x$" reactions, were the main path of N_2O production. The introduction of Ni could avoid the occurrence of non-selective catalytic "$NH_3 + O_2 + NO_x$" reaction and reduce the amount of N_2O production in SCR process. While "$NH_3 + O_2$" reaction was the main reaction to produce N_2O for $Ni_1Mn_{0.5}Al_{0.5}O_x$, which showed the lower N_2O production amount, occupying higher N_2 selectivity.

3.5. Surface physicochemical properties of catalysts

XPS analysis was performed to explore the chemical composition and surface element valence of catalysts (Fig. 4). In the O1s XPS spectra of three catalysts, two peaks due to the lattice oxygen (O_β, 529.7–530 eV), and the surface adsorbed oxygen (O_α, 531.3 eV) could be obtained. Due
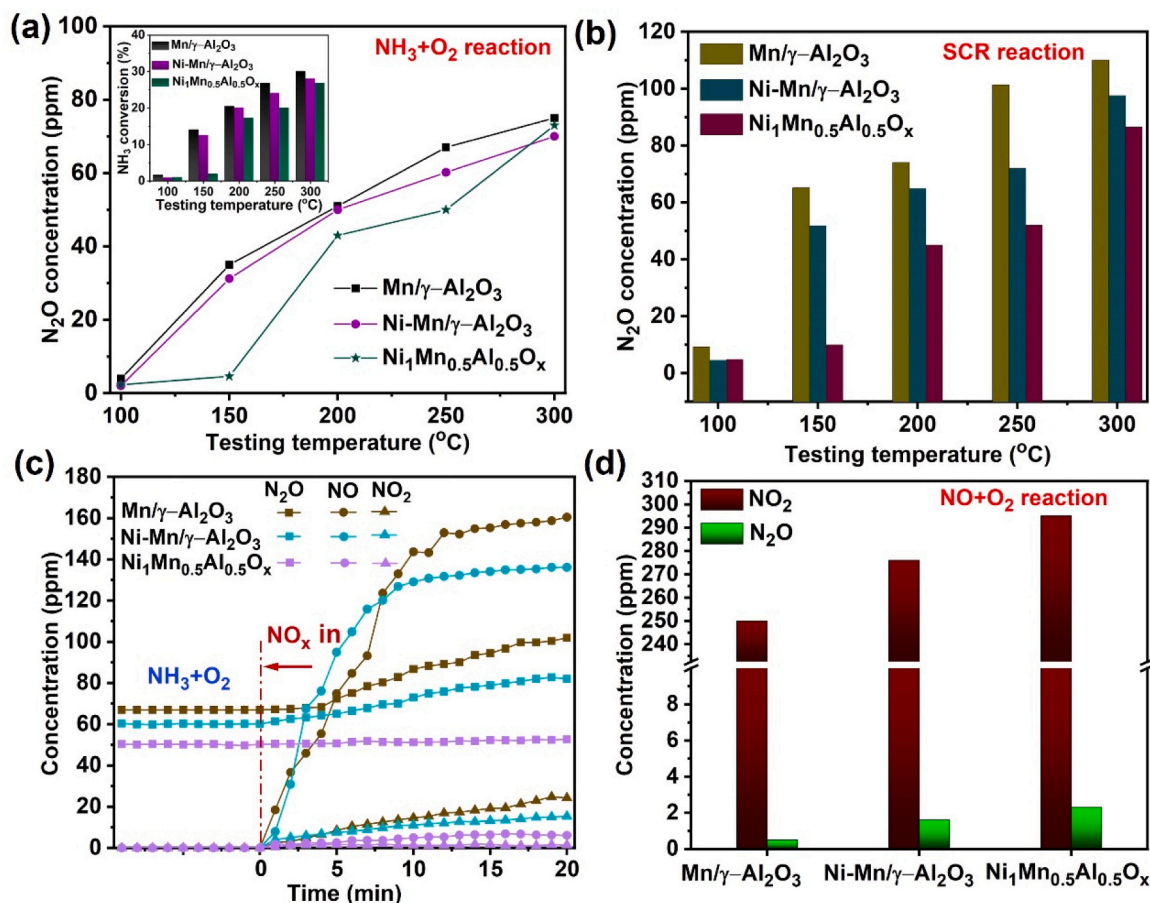
Fig. 3. (a) N_2O concentration of NH_3 oxidation reaction and the inset figure is the NH_3 conversion on the catalysts, (b) N_2O concentration of SCR reaction, (c) Transient reaction results, and (d) NO_x oxidation reaction results over Mn/γ-Al$_2$O$_3$, Ni-Mn/γ-Al$_2$O$_3$ and Ni$_1$Mn$_{0.5}$Al$_{0.5}$O$_x$. Reaction conditions: [NO_x] = [NH_3] = 500 ppm, [O_2] = 5%, balance Ar, total flow rate = 200 mL/min, GHSV = 60,000 h^{-1}, catalyst 0.15 g.

to the higher mobility, O_α has higher activity in catalytic reactions than O_β [41]. After the introduction of Ni, the $O_\alpha/(O_\alpha + O_\beta)$ atom-% fraction was increased following: Ni$_1$Mn$_{0.5}$Al$_{0.5}$O$_x$ (53.9%) > Ni-Mn/γ-Al$_2$O$_3$ (49.1%) > Mn/γ-Al$_2$O$_3$ (43.6%). A higher proportion of $O_\alpha/(O_\alpha + O_\beta)$ favored the oxidation of NO, which led to the occurrence of "fast-SCR" reaction (4NH$_3$ + 2NO + 2NO$_2$ → 4 N$_2$ + 6 H$_2$O).

The XPS analysis of Mn 2p showed that MnO$_x$ species existed in a mixed valence in all samples with two main peaks (Fig. 4b). For Mn 2p3/2 peak, three peaks could be obtained, which were assigned to Mn^{4+} (~643.3 eV), Mn^{3+} (~641.6 eV), and Mn^{2+} (~637.5 eV), respectively. For Mn-based catalysts, the catalytic cycle between Mn^{4+} and Mn^{3+}(MnO$_2$→Mn$_2$O$_3$ +O*) was beneficial to the SCR reaction. Importantly, the total amount of Mn^{4+} and Mn^{3+} was increasing with the introduction of Ni. Since Mn^{4+} was more susceptible to oxidation on Mn-based catalysts, it has an important role in catalytic reactions [32,42]. Obviously, the Mn^{4+}/(Mn^{4+}+Mn^{3+}+ Mn^{2+}) atom-% fraction appeared to increase and followed the order of Ni-Mn/γ-Al$_2$O$_3$ (61.9%) > Ni$_1$Mn$_{0.5}$Al$_{0.5}$O$_x$ (51.2%) > Mn/γ-Al$_2$O$_3$ (45.8%), and a moderate amount of Mn^{4+} species can avoid excessive oxidation of NH$_3$, thereby increasing N$_2$ selectivity.

In Fig. 4c, four peaks were mainly observed at 848–883 eV, which was due to Ni 2p3/2 and Ni 2p1/2 accompanied by two satellite peaks. Ni 2p3/2 could be fitted into two peaks, corresponding to Ni^{3+} (~855.6 eV) and Ni^{2+} (~854.3 eV). For Ni$_1$Mn$_{0.5}$Al$_{0.5}$O$_x$ and Ni-Mn/γ-Al$_2$O$_3$, the Ni^{2+}/(Ni^{3+}+ Ni^{2+}) atom-% fraction was 41.6% and 39.1%, respectively. Ni^{2+} species were preferred for redox reactions and played an important role in improving SCR performance, which may be the electron transfer between Ni^{2+} and Mn^{4+} in a process similar to Mn^{4+} +

Ni^{2+} ↔ Mn^{3+} + Ni^{3+} [43]. Therefore, the relatively high contents of Mn^{4+}, Ni^{2+} and O$_\alpha$ in Ni$_1$Mn$_{0.5}$Al$_{0.5}$O$_x$ promoted its excellent catalytic activity. According to ICP-MS test and XPS analysis, the Mn and Mn^{4+} contents were obtained. In Fig. 4d, the Mn content of Mn/γ-Al$_2$O$_3$, Ni-Mn/γ-Al$_2$O$_3$ and Ni$_1$Mn$_{0.5}$Al$_{0.5}$O$_x$ catalysts was 1.8%, 0.9% and 14.6% respectively, which was similar to the dosage of preparation. In addition, Ni$_1$Mn$_{0.5}$Al$_{0.5}$O$_x$ has more highly dispersed Mn^{4+}species, which was beneficial to LT-SCR reaction. Compared with Mn/γ-Al$_2$O$_3$ (135.5 m^2/g) and Ni-Mn/γ-Al$_2$O$_3$ (186.28 m^2/g), the introduction of Ni could effectively increase the specific surface area of the sample (Table S1). In addition, the specific surface area of LDOs obtained by high temperature calcination of LDHs became larger. Especially, Ni$_1$Mn$_{0.5}$Al$_{0.5}$O$_x$ possessed the largest specific surface area (374.15 m^2/g), which facilitated the adsorption of NO$_x$ and NH$_3$ reactants.

In order to study the effect of Ni doping on the reducibility of the catalyst, H$_2$-TPR experiments of the catalyst were performed (Fig. 5a). For the control Mn/γ-Al$_2$O$_3$ sample, two H$_2$-TPR peaks were around ~263 and 567 $^\circ$C, which may be attributed to the following successive reduction steps: MnO$_2$→Mn$_2$O$_3$→Mn$_3$O$_4$→MnO [22,44]. For the Ni$_1$Mn$_{0.5}$Al$_{0.5}$O$_x$ and Ni-Mn/γ-Al$_2$O$_3$, two broad peaks were still observed. Compared with the H$_2$-TPR curve of Mn/γ-Al$_2$O$_3$, the temperature of the first reduction peak of Ni$_1$Mn$_{0.5}$Al$_{0.5}$O$_x$ shifted to the lower temperature. The second reduction peak at high temperature (567–644 $^\circ$C) may be due to the superposition of the reduction of Ni^{3+}→Ni^{2+}→Ni^0 and MnO$_x$ species. In addition, the H$_2$-TPR peak areas of Ni-Mn/γ-Al$_2$O$_3$ and Ni$_1$Mn$_{0.5}$Al$_{0.5}$O$_x$ were larger than that of Mn/γ-Al$_2$O$_3$. The H$_2$ consumptions of samples were quantified through a pulse experiment,
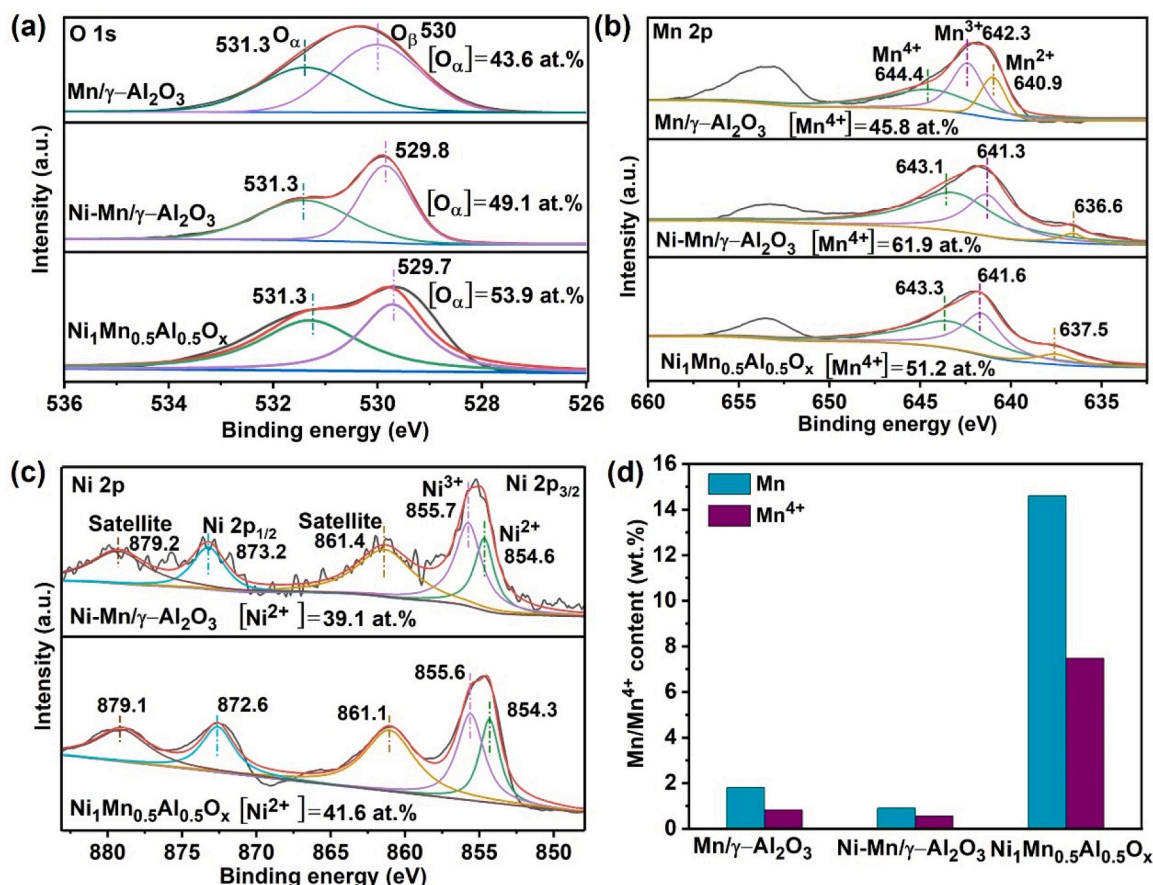
Fig. 4. XPS results of (a) O 1 s, (b) Mn 2p, and (c) Ni 2p over catalyst; (d) Mn/Mn^{4+} content of catalysts.

which followed the sequence of Ni$_1$Mn$_{0.5}$Al$_{0.5}$O$_x$ (2.15 mmol/g) > Ni-Mn/γ–Al$_2$O$_3$ (0.45 mmol/g) > Mn/γ–Al$_2$O$_3$ (0.18 mmol/g). The improvement may be attributed to the synergistic influence between Ni and Mn species. Therefore, combined with the reduction peak temperature and H$_2$ consumption, Ni$_1$Mn$_{0.5}$Al$_{0.5}$O$_x$ prepared by LDH calcination has higher Mn and Cu species reduction ability, which means that the surface oxygen mobility increased and the SCR reaction proceeded rapidly.

It was well known that the reaction between adsorbed NH$_3$ and adsorbed NO species was the main reaction at low temperature (L-H mechanism). So, the NO-TPD analysis of all samples were shown in Fig. 5b, and all samples showed two desorption peaks. The peaks at low temperature (~200 ^{o}C) could be attributed to the desorption of monodentate nitrate species, while the peaks at high temperature (~500 ^{o}C) were the desorption of bidentate/bridged nitrate species [4,45]. Notably, Ni$_1$Mn$_{0.5}$Al$_{0.5}$O$_x$ showed the largest desorption peak area, especially at low temperatures, indicating that it had the highest adsorption capacity for NO. In addition, NH$_3$-TPD analysis of all samples were studied (Fig. 5c). For the control Mn/γ–Al$_2$O$_3$ sample, two desorption peaks were displayed at ~142 and 493 ^{o}C, assigned to weak and strong acid sites, respectively. With the introduction of Ni species, a distinct new desorption peak appeared at ~336 ^{o}C, corresponding to medium acid sites. The amounts of desorbed NH$_3$ (surface acidity) over Ni$_1$Mn$_{0.5}$Al$_{0.5}$O$_x$, Ni-Mn/γ–Al$_2$O$_3$, and Mn/γ–Al$_2$O$_3$ were compared by integrating the NH$_3$-TPD curves (Fig. 5d), which followed the order of Ni$_1$Mn$_{0.5}$Al$_{0.5}$O$_x$ (240.5 μmol/g) > Ni-Mn/γ–Al$_2$O$_3$ (137.2 μmol/g) > Mn/γ–Al$_2$O$_3$ (105.1 μmol/g). Ni$_1$Mn$_{0.5}$Al$_{0.5}$O$_x$ catalyst was visible larger than that of the control samples, which suggested that the addition of Ni species increased the amount of acid sites, and significantly improved the adsorption capacity of NH$_3$.

3.6. In situ DRIFTS studies

After exposure to 1000 ppm NH$_3$/N$_2$ at 200 ^{o}C for different times, the adsorption of NH$_3$ on Mn/γ–Al$_2$O$_3$ and Ni$_1$Mn$_{0.5}$Al$_{0.5}$O$_x$ were studied by in-situ DRIFTS (Fig. 6a, b). the characteristic peaks of amide (–NH$_2$) species (1556, and 1531 cm^{-1}) [46,47], NH$_4^+$ (1690, and 1694 cm^{-1}) bonded to Brønsted acid sites [46], and coordinated NH$_3$ (1617, 1622, 1177, and 1261 cm^{-1}) linked to Lewis acid sites appeared with time increase [48]. Besides, the peak corresponding to the –NH species (1461 cm^{-1}) appeared in the DRIFTS spectra of NH$_3$ adsorption over Mn/γ–Al$_2$O$_3$ catalyst, which was caused by excessive hydrogen absorption of NH$_3$, but can hardly be found in the spectrum of catalyst Ni$_1$Mn$_{0.5}$Al$_{0.5}$O$_x$ [46]. Liu et al. [49] and Kapteijn et al. [15] reported that the –NH species were unable to react with NO to form N$_2$ instead of N$_2$O species. The peak intensity of adsorbed NH$_3$ species indicated that the introduction of Ni could improve the adsorption behavior of NH$_3$ on the catalyst surface. The adsorption and activation of NH$_3$ could be promoted by the synergistic effect due to Ni doping, which was consistent with the results of NH$_3$-TPD (Fig. 5c).

Fig. 6c, d showed the in-situ DRIFT spectra of Mn/γ–Al$_2$O$_3$ and Ni$_1$Mn$_{0.5}$Al$_{0.5}$O$_x$ catalysts exposed to 2000 ppm NO+ 5% O$_2$/Ar gas flow. The adsorbed NO$_2$ species (1612, 1622 cm^{-1}) [50], bidentate nitrate (1551–1582 cm^{-1}) [51,52], monodentate nitrate species (1254, 1277, 1310 cm^{-1}) were observed [53], where the peaks of chelating nitrite and bridging nitrate overlapped [52]. The bidentate nitrate and monodentate nitrate increased with increasing temperature. Comparing the peak intensity of NO$_x$ species, Ni$_1$Mn$_{0.5}$Al$_{0.5}$O$_x$ was stronger than Mn/γ–Al$_2$O$_3$, indicating that Ni and Mn have a better ability to adsorb and activate NO$_x$. Therefore, it was evident that the doping of Ni enriched the active sites for adsorption and activation of reactive species, and accelerated the NH$_3$-SCR process on the surface of
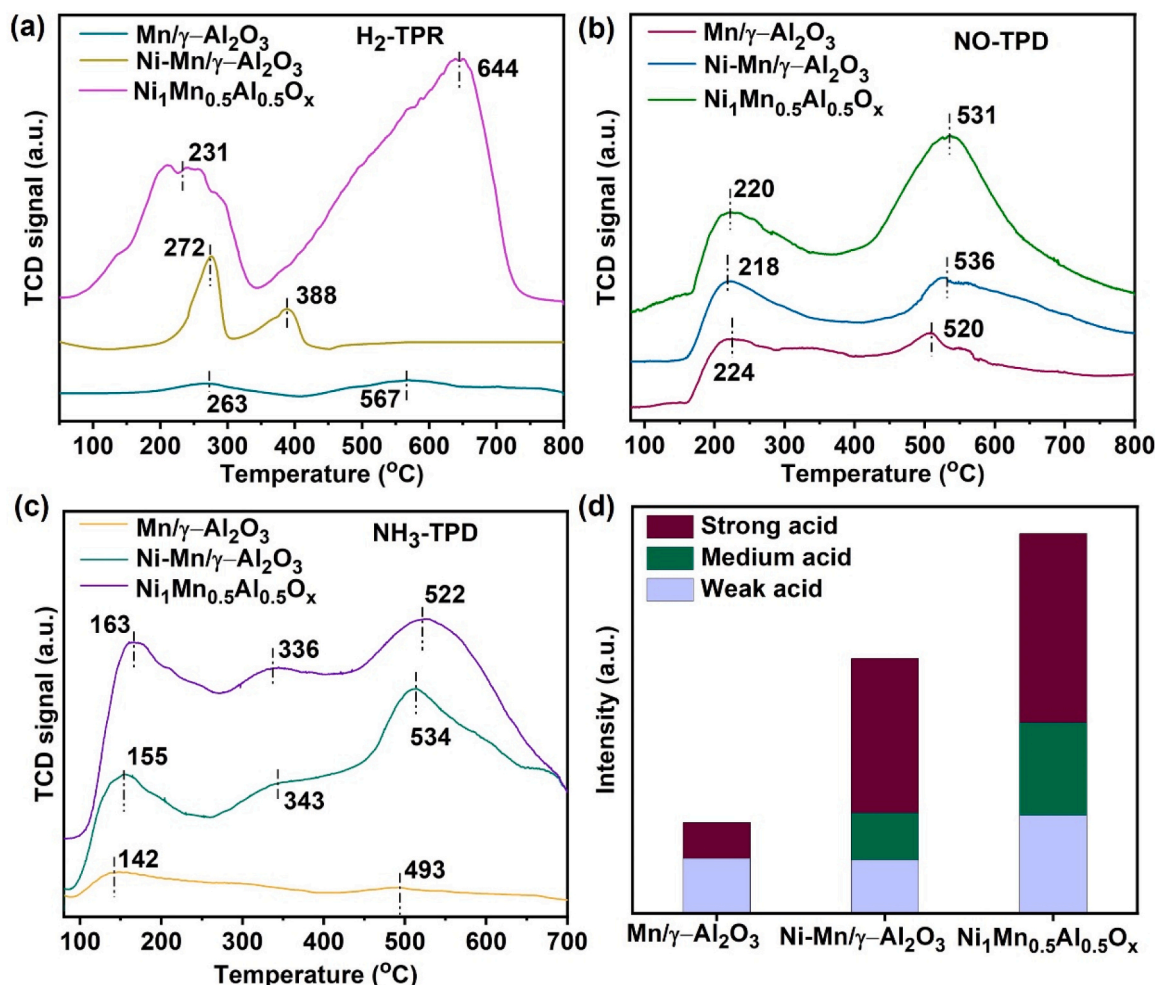
Fig. 5. (a) H_2-TPR profiles, (b) NO-TPD profiles, (c) NH_3-TPD profiles, (d) surface acidity distribution over different catalysts; In situ DRIFTS spectra obtained after a 30 min exposure to 1000 ppm NH_3 over (e) Mn/γ-Al_2O_3, (f) $Ni_1Mn_{0.5}Al_{0.5}O_x$ catalysts at 200 °C; In situ DRIFTS spectra obtained after a 30 min exposure to 2000 ppm NO + 5% O_2 over (g) Mn/γ-Al_2O_3 (h) $Ni_1Mn_{0.5}Al_{0.5}O_x$ catalysts at 200 °C.

$Ni_1Mn_{0.5}Al_{0.5}O_x$ catalyst.

In-situ DRIFTS study of NO + O_2 reaction with pre-adsorbed NH_3 was recorded at 200 °C, as illustrated in Fig. 7. After introducing NO+ O_2 in the reaction cell, these bands assigned to the adsorbed NH_3 species gradually weaken and disappeared, while those peaks ascribing to the adsorbed NO_x species of Mn/γ-Al_2O_3 (1307, 1540, 1559, 1585, and 1614 cm^{-1}) and $Ni_1Mn_{0.5}Al_{0.5}O_x$ (1252, 1277, 1544, 1573, and 1617 cm^{-1}) gradually emerged with time (Fig. 7a, b) [54]. The difference was that more NH_3 species adsorbed on $Ni_1Mn_{0.5}Al_{0.5}O_x$ was consumed than Mn/γ-Al_2O_3. The above results revealed that the reaction of gaseous NO + O_2 and pre-adsorbed NH_3 can proceed through the E-R mechanism on the both catalysts. In comparison, $Ni_1Mn_{0.5}Al_{0.5}O_x$ presented a better activating ability of NH_3 than Mn/γ-Al_2O_3, which could accelerate more active NH_3 species to react with NO_x, thereby enhancing the NH_3-SCR performance.

The reactivity of NH_3 with pre-adsorbed NO + O_2 was investigated at 200 °C by DRIFTS analysis, as presented in Fig. 7c, d. After pretreatment by NO + O_2, various bands assigned to adsorbed NO_x species could be found both in the spectra of Mn/γ-Al_2O_3 and $Ni_1Mn_{0.5}Al_{0.5}O_x$. The bands of adsorbed NO_x species quickly decreased in intensity and all bands nearly vanished when NH_3 was added in for 10 min. Additionally, the bands ascribing to adsorbed NH_3 species of Mn/γ-Al_2O_3 (1311, 1534, 1543, 1559, 1565, and 1609 cm^{-1}) and $Ni_1Mn_{0.5}Al_{0.5}O_x$ (1184, 1252, 1278,1520 and 1610 cm^{-1}) arose after 2 min [55]. The above observations suggested that the rection of NH_3 and pre-adsorbed NO_x species could occur on these two catalysts via L-H mechanism. Combined with

DRIFTS adsorption and NH_3/NO-TPD result (Fig. 5), the Ni doping enhanced the total amount of NH_3 and NO_x adsorbed on $Ni_1Mn_{0.5}Al_{0.5}O_x$, which can accelerate the SCR process via the L-H and E-R mechanisms.

3.7. DFT calculations

DFT was used to calculate in depth the properties of the catalyst surface. The charge density difference plots for Mn/γ-Al_2O_3 and NiMnAlO$_x$ catalysts were employed to detect the catalysts surface. In Fig. 8a, b, oxygen accepted electrons from Mn in Mn/γ-Al_2O_3 catalyst, implicating that Mn atoms and oxygen atoms were connected by ionic bounds. For Mn$_{5c}$ site, larger cyan areas appeared at its center and top, belonging to its un-occupation orbit. The un-occupation orbit could accommodate additional electrons, which can be responsible for Lewis acid site [56], thus, Mn$_{5c}$ showed strong Lewis acidity. The charge density difference plots for Ni doping of NiMnAlO$_x$ catalyst was shown in Fig. 8c, d. The apparent electrons transfer could be found between Mn atom and oxygen atom. Electrons were also observed accumulating between Mn$_{3c}$ and oxygen atom, and a few electrons accumulated at the center of Mn$_{3c}$. In addition,

Mn$_{3c}$ was surrounded by a flower-like electron loss region with a small amount of unoccupied orbits present, contributing to the generation of moderate Lewis acids in the NiMnAlO$_x$ catalyst, and this result corroborated the result of TPD experiment. Strong electron transition could be found between Mn atom and oxygen atom, or Ni atom and
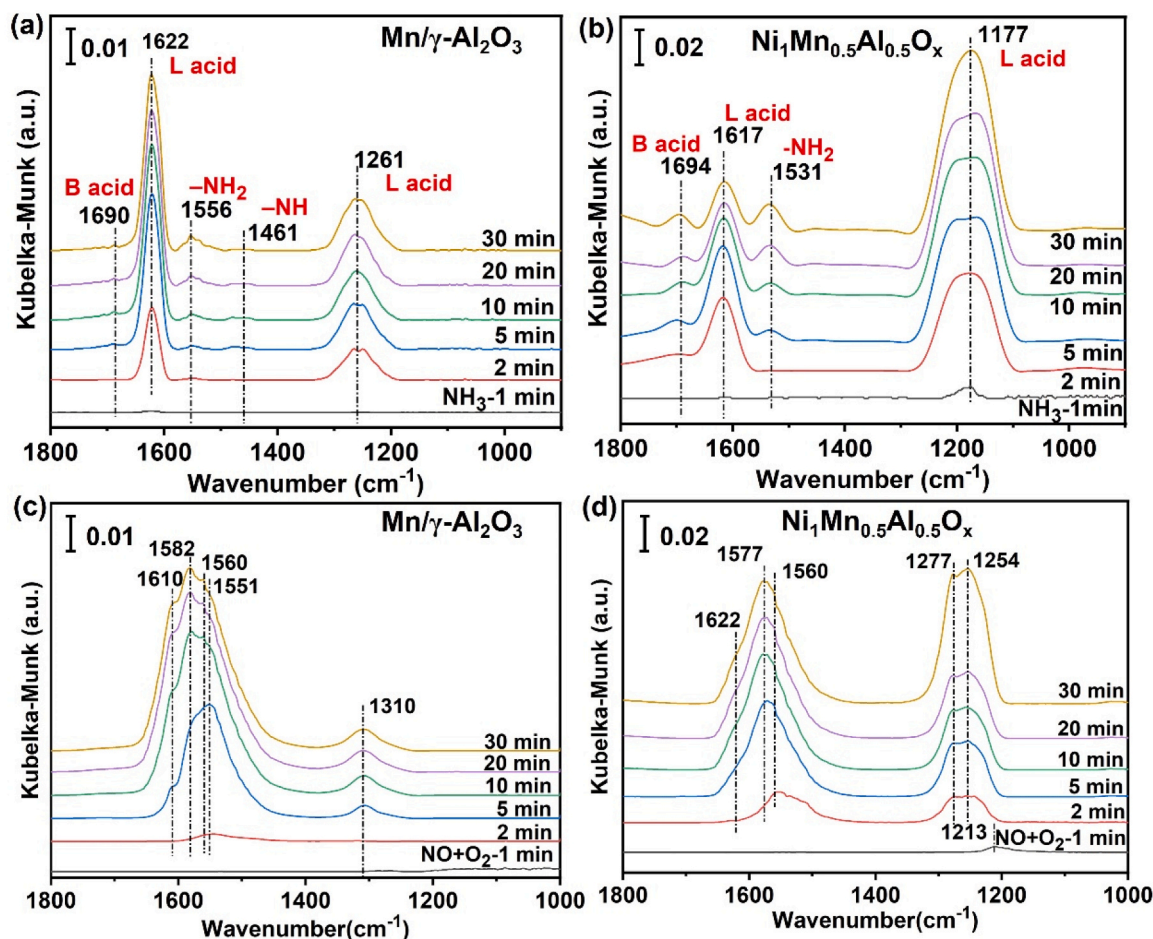
Fig. 6. In situ DRIFTS spectra obtained after a 30 min exposure to 1000 ppm NH_3 over (a) Mn/γ-Al_2O_3, (b) $Ni_1Mn_{0.5}Al_{0.5}O_x$ catalysts at 200 °C; In situ DRIFTS spectra obtained after a 30 min exposure to 2000 ppm NO + 5% O_2 over (c) Mn/γ-Al_2O_3 (d) $Ni_1Mn_{0.5}Al_{0.5}O_x$ catalysts at 200 °C.

oxygen atom on $NiMnAlO_x$ surface, which may lead to change in valence of Mn and Ni ions through the process of $Mn^{4+} + Ni^{2+} \leftrightarrow Mn^{3+} + Ni^{3+}$.

PDOS analysis of the d-band of Mn showed that the d-band of Mn of $NiMnAlO_x$ was more localized and had a greater degree of spin polarization compared to the d-band of Mn/γ-Al_2O_3 (Fig. 8e). The d-band of Mn/γ-Al_2O_3 had a low bandwidth of spins broadly distributed between − 6 and 3 eV, whereas the d-band of $NiMnAlO_x$ had a localized and narrow peak near − 5 to − 2 eV, so that more active electrons were available for the Mn site in $NiMnAlO_x$ oxides to participate in the interaction. The d up spin of $NiMnAlO_x$ had a small peak only at the Fermi level for a small unoccupied orbital, indicating that the d upward spin was weakly acidic, in agreement with the charge density difference results. The d-band down spins of both $NiMnAlO_x$ and Mn/γ-Al_2O_3 existed unoccupied orbitals, suggesting that both of their down spins exhibited electron-acquiring ability and acidity. But there were fewer occupied state orbitals in the d-band down spins of $NiMnAlO_x$. Interestingly, these phenomena were also reflected in the coordination field effects of Mn (Fig. 8f-h). The d-band suborbital energy levels of Mn split in Mn/γ-Al_2O_3 showed a high degree of degeneracy than in $NiMnAlO_x$. The energy gap between the t_{2g} and e_g orbitals in the up and down spins of the d-band of Mn in the Mn/γ-Al_2O_3 system was about 0.1 eV and 0.4 eV, respectively, indicating that there was an obvious Jahn-Teller effect for the Mn element in Mn/γ-Al_2O_3. In contrast, the t_{2g} and e_g orbitals in the up and down spins of the d-band of Mn in $NiMnAlO_x$ were highly degenerated, leading to the disappearance of the energy gap between the t_{2g} and e_g orbitals, and this Jahn-Teller degradation explained the localized and intensified d-band of Mn in $NiMnAlO_x$ [37].

The E_{ads} of NH_3 and NO on the Mn/γ-Al_2O_3 (110) and $NiMnAlO_x$

(111) surface were evaluated (Fig. 9). The result showed that the adsorption reactions of NH_3 molecular on Mn/γ-Al_2O_3 and $NiMnAlO_x$ catalysts were exothermic reaction, with E_{ads} of − 1.27 eV and − 1.17 eV and bond lengths of 2.05 Å and 2.20 Å, respectively, suggesting that NH_3 and Mn/γ-Al_2O_3 catalyst had strong bonding ability. The Mn sites served as Lewis acid site in these two configurations, and the lower adsorption energy indicated that Ni specie may weaken the strong surface Lewis acidity to moderate surface Lewis acid of $NiMnAlO_x$ catalyst. According to the literature and the result of our transient kinetics studies, the N_2O formation in NH_3-SCR reaction was mainly through NH_3 oxidation pathway [57]. More moderate Lewis acidity of Mn active site may lead to less N_2O formation via NH_3 oxidation pathway.

The E_{ads} of NO on the surface Mn site enhanced from 0.22 eV to − 0.78 eV, and bond length decreased from 2.36 Å to 1.76 Å on the Mn/γ-Al_2O_3 (110) and $NiMnAlO_x$ (111), respectively. The higher E_{ads} for NO on the $NiMnAlO_x$ (111) indicated that the Ni species greatly enhanced the interaction between NO and Mn site, well supporting the view that Ni increased the active sites for adsorption and activation, as mentioned in DRIFT and NO-TPD experiments. For absolute value of adsorption energy was more than − 0.3 eV, NH_3 and NO molecular can be chemisorbed over the surface of $NiMnAlO_x$ (111), while NO cannot be adsorbed on the Mn/γ-Al_2O_3 (110). Comparing the adsorption energy between NO and NH_3, NH_3 adsorption energy was higher on Mn/γ-Al_2O_3 (110) surface but lower on $NiMnAlO_x$ surface, which indicated that NH_3-SCR reaction preferred L-H reaction route while doping Ni on $NiMnAlO_x$ LDO. Moreover, NH_3-SCR on catalyst at low temperature followed L-H mechanism more effectively.

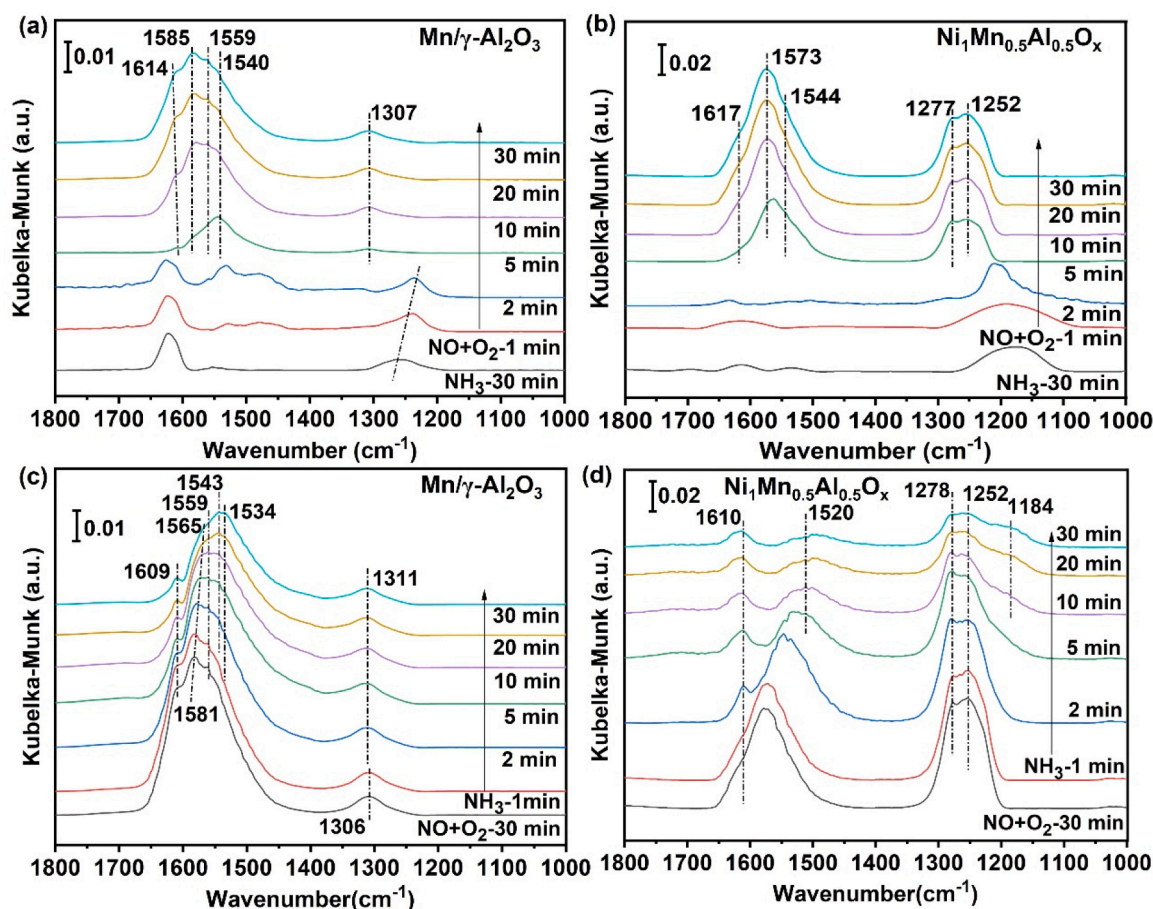**Fig. 7.** In situ DRIFTS spectra of the reaction between 2000 ppm NO + 5% O_2 and pre-adsorbed NH_3 over (a) Mn/γ-Al_2O_3 and (b) $Ni_1Mn_{0.5}Al_{0.5}O_x$ and 1000 ppm NH_3 reacting with pre-adsorbed NO + O_2 over (c) Mn/γ-Al_2O_3 and (d) $Ni_1Mn_{0.5}Al_{0.5}O_x$ at 200 °C.

Interestingly, we found that the adsorption of small molecular on the NiMnAlO$_x$ catalyst was accompanied by a magnetic moment reversal of the active center and the catalyst as a whole, which permitted the Mn active center to interact with the small molecule in an electronic state more favorable for small molecule reactions [58]. In contrast to the ferromagnetism of system Mn/γ-Al_2O_3, the anti-ferromagnetism of system NiMnAlO$_x$ allowed the doping Mn active sites therein to switch between opposite magnetic moments. The Ni site in the anti-ferromagnetic bulk of NiO had opposite magnetic moments of − 1.82 and 1.82 μB (Fig. 10a). The antiferromagnetic cell of NiO allowed for opposite magnetic moments between two adjacent layers of Ni atoms in its (111) surface (Fig. 10b), with the surface Ni atomic layer having a magnetic moment at ~1.4 μB relative to the deeper Ni. When Mn was doped into the superficial atomic Ni layer on the surface of NiO (111), Mn and the co-layered Ni atoms exhibited opposite magnetic moments due to the large magnetic moment (4.32 μB) of Mn (Fig. 10c), which made the magnetic moment of the Mn site easily reversed (Fig. 10d). The reversal of the magnetic moments of the Mn sites led to the reversal of the magnetic moments of the same layer of Ni and the adjacent layer of Ni, which will lead to the reversal of the magnetic moment of the catalyst as a whole. This reversal of magnetic moment occurred when the catalyst adsorbed paramagnetic NO (Fig. 10f), which made the binding of NO to Mn site stronger, as evidenced by a significant increase in the adsorption energy of NO at Mn site. The binding of NO to Mn site weakened the huge magnetic moment of Mn site, which led to the stability of the overall antiferromagnetic state of the catalyst. In contrast, the interaction of the non-magnetic NH_3 with the Mn site did not have this magnetic moment reversal and did not cause the magnetic moment of the Mn site weakened (Fig. 10e), which also prevented the

over-bonding of NH_3 and Mn. In ferromagnetic Mn/γ-Al_2O_3, the interaction of the Mn site with NH_3 slightly weakened the magnetism of the adsorbed site, which may be due to over-bonding of NH_3 to the Mn site. The weak interaction of NO with Mn of Mn/γ-Al_2O_3 did not change the magnetic moment of Mn, while the interaction caused NO to take on the up magnetic moment in ferromagnetic system.

In order to gain insight into the mechanism and influence of the degradation of the Jahn-Teller effect and magnetic moment reversal of Mn sites on the surface adsorption process, the partial density of state (PDOS) for NO/NH_3 adsorption models of Mn/γ-Al_2O_3 and NiMnAlO$_x$ were investigated (Fig. 11). For NO adsorption, the π * orbital resonated only slightly with the broad d-band up spin of Mn/γ-Al_2O_3 about the Fermi level (Fig. 11a). While for NO adsorbed on Mn site of NiMnAlO$_x$ surface, not only the π * orbital interacted with both up spin and down spin of the localized d band, but also the π orbital involved in the bonding with down spin of d band, which was indicated by the π-d bonding and (π-d)* bonding at − 6.6 eV and − 2.7 eV, respectively. This bonding mode was due to the reversal of the magnetic moment of the Mn site in NiMnAlO$_x$ upon NO adsorption, which caused the d-band up spin to become a state with a large number of empty orbitals, while the electron-accessing ability of the empty orbitals was further strengthened by the effect of the Jahn-Teller degeneracy, thus permitting single electrons on the π * orbitals in NO to enter into empty orbitals on the d-band up spin for interactions. Similarly, the down spin of Mn d band after the magnetic moment reversal had active electrons that could be injected into the down spin empty orbitals of π * of NO and could interact with the π orbitals to form a series of bonding and antibonding orbitals. Consequently, the multiple bonding between NO molecule and NiMnAlO$_x$ markedly enhanced the NO chemisorption. Fig. 11c,
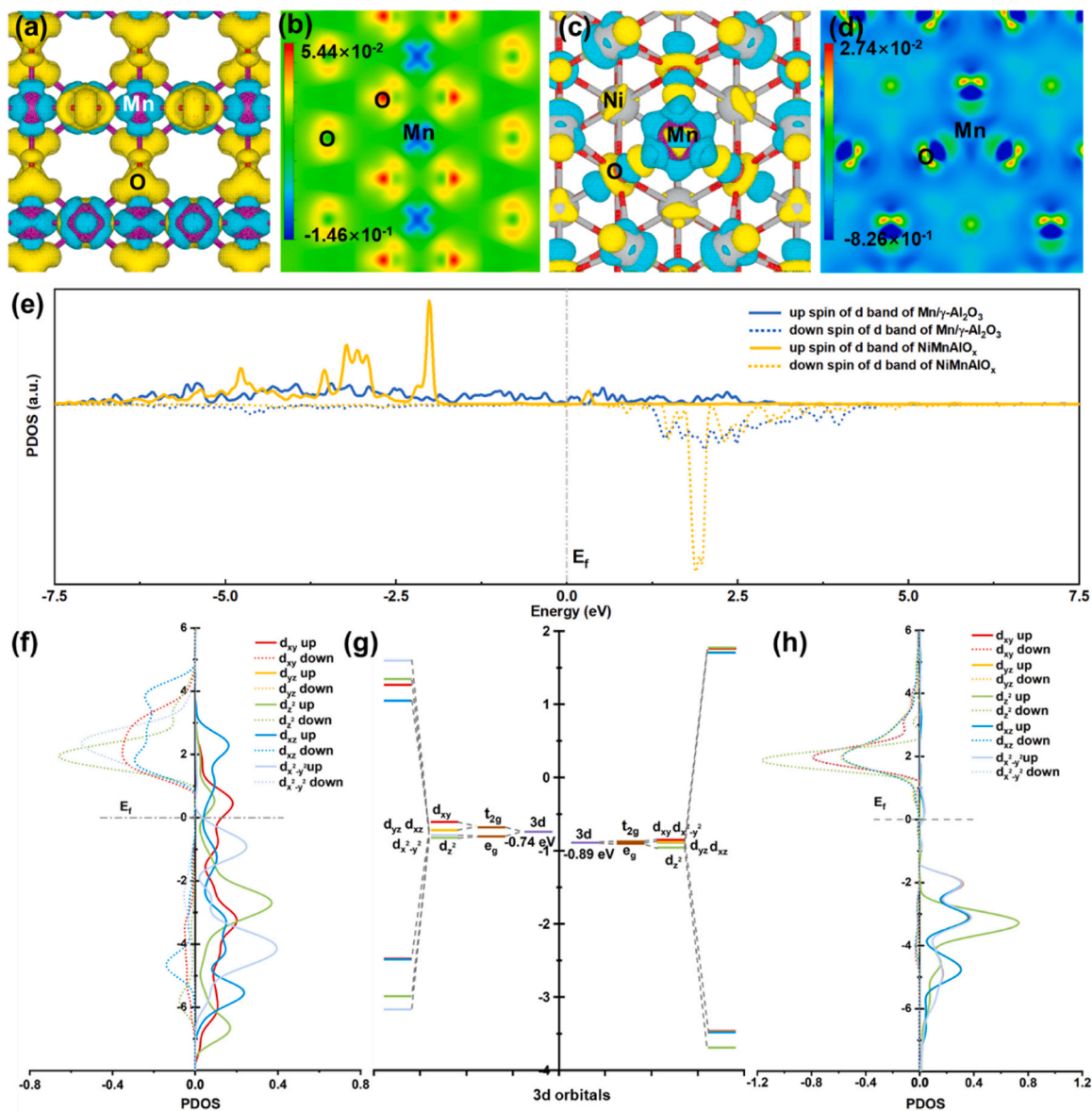
Fig. 8. The charge density difference plots and 2D display of (a, b) Mn/γ-Al$_2$O$_3$ and (c, d) NiMnAlO$_x$. Cyan area represents loss of electron, yellow area represents gain of electron. (e) PDOS profiles of the Mn site of Mn/γ-Al$_2$O$_3$ and NiMnAlO$_x$, 3d orbital-resolved PDOS profiles for Mn site on (f) clean Mn/γ-Al$_2$O$_3$ and (h) NiMnAlO$_x$, (g) schematic band structure of the Mn site, the left and right side of the vertical axis belong to Mn/γ-Al$_2$O$_3$ and sulfated NiMnAlO$_x$, respectively.
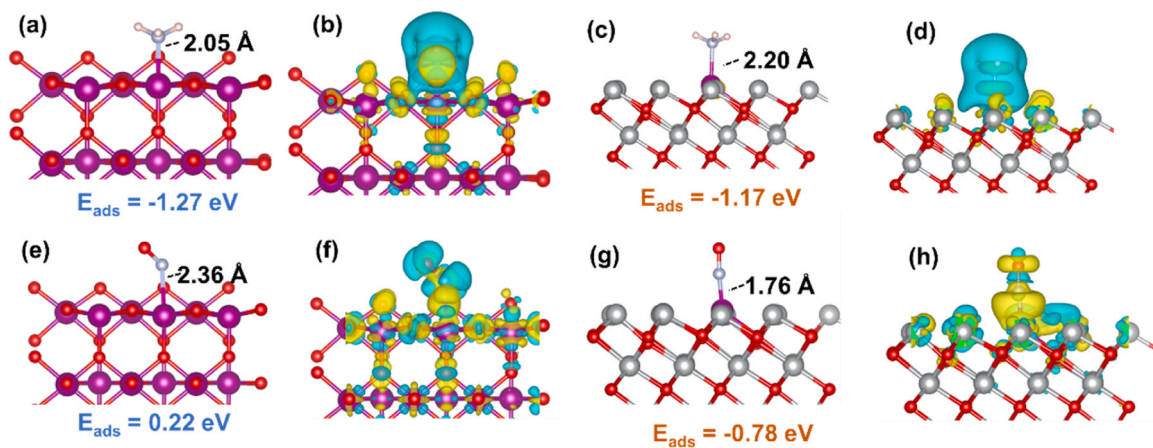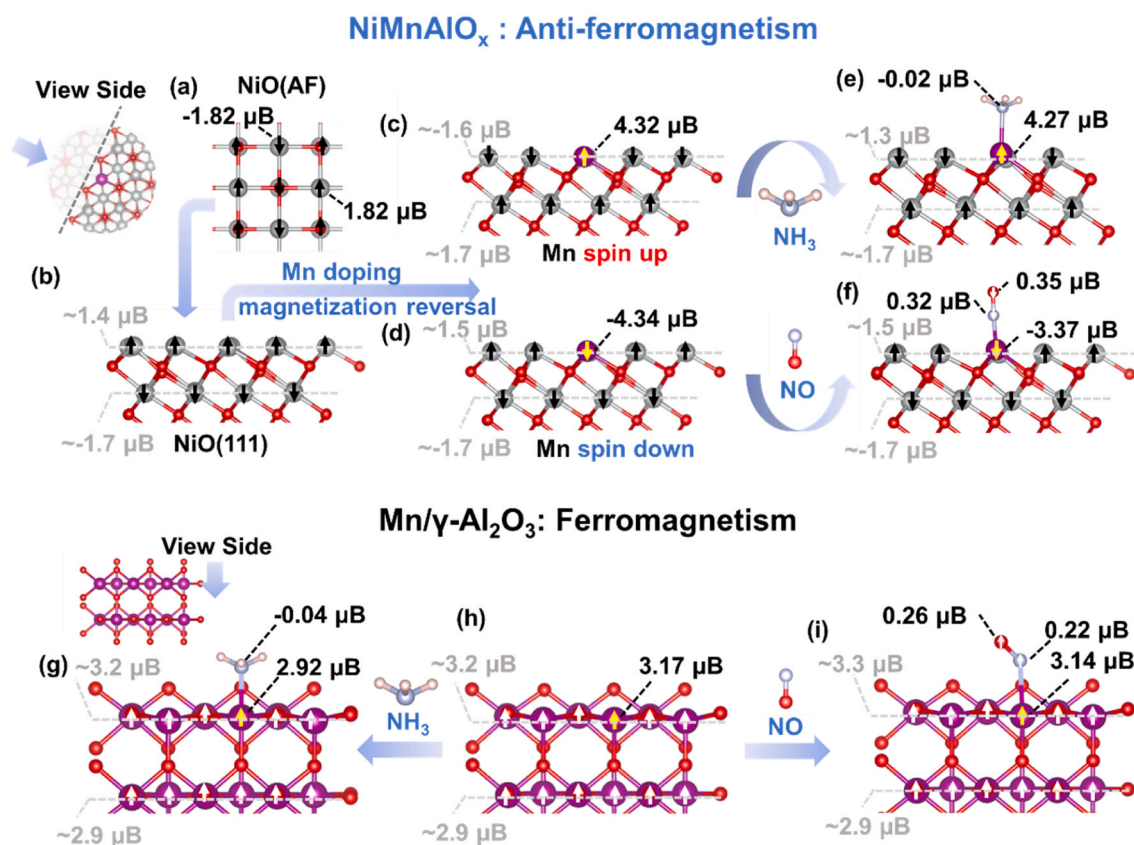

Fig. 9. Optimized configurations and corresponding charge density differences of NO and NH$_3$ adsorbed on (a, b and e, f) Mn/γ-Al$_2$O$_3$ and (c, d and g, h) NiMnAlO$_x$.

Fig. 10. Schematic diagram of the magnetization reversal process during small molecular adsorption on Mn/γ-Al$_2$O$_3$ and NiMnAlO$_x$ and the magnetic moment diagram of (a) NiO bulk, (b) NiO (111), (c) clean and (e) NH$_3$ adsorption on NiMnAlO$_x$ with up-magnetic moment Mn site, (d) clean and (f) NO adsorbed on NiMnAlO$_x$ with down-magnetic moment Mn site, and (h) clean, (g) NO, and (i) NH$_3$ adsorbed on Mn/γ-Al$_2$O$_3$.

d compared the bonding state of NH$_3$ molecule adsorbed on Mn/γ-Al$_2$O$_3$ and NiMnAlO$_x$ surfaces. The n orbitals of NH$_3$ shifted to the low energy level after bonding to the Mn site of Mn/γ-Al$_2$O$_3$, with the broaden n-d bonding and (n-d)* anti-bonding evolved in up spin. Analogously, the d band of Mn of NiMnAlO$_x$ surfaces exhibited an obvious interaction with the n orbitals of NH$_3$. However, the Jahn-Teller degradation led to the localization of the up spin on the d band and the reduction of the empty orbitals, so that the (n-d)* anti-bonding orbitals were below the Fermi level, suggesting the filling of electrons, and simultaneously the reduction of resonance of the down spin n and d bands, which reduced the stability of the incorporation between NH$_3$ and NiMnAlO$_x$. In addition, compared to Mn/γ-Al$_2$O$_3$, the d band of the Mn atom of NiMnAlO$_x$ shifted to higher energy level after combining with NH$_3$. These also further explained the lower adsorption energy for NH$_3$ on NiMnAlO$_x$ than on Mn/γ-Al$_2$O$_3$.

4. Conclusions

In this work, the overall catalytic performance of LDHs-derived NiMnAlO$_x$ were studied in the NH$_3$-SCR reaction of NO$_x$. The preferred Ni$_1$Mn$_{0.5}$Al$_{0.5}$O$_x$ exhibited excellent LT-SCR catalytic activity with a NO$_x$ conversion of exceeded 95% at 100–250 °C. In the transient reaction, we demonstrated that the Ni-modified Ni$_1$Mn$_{0.5}$Al$_{0.5}$O$_x$ catalyst could effectively inhibit the non-selectively catalytic "NH$_3$ +O$_2$ +NO" pathway to generate N$_2$O and improve the selectivity of N$_2$. SO$_2$ TPD analyses showed that Ni$_1$Mn$_{0.5}$Al$_{0.5}$O$_x$ catalyst has better SO$_2$ resistance with less formation of sulfate species. The NH$_3$-TPD, H$_2$-TPR and in-situ DRIFTS results indicated that the appropriate amount of Ni modified Ni$_1$Mn$_{0.5}$Al$_{0.5}$O$_x$ catalyst could modulate the surface acidity, redox properties as well as the adsorption and activation active sites. In DFT calculations, charge density difference analysis revealed the

presence of strong electron leaps between atoms as well as intermetallic synergies. The adsorption energy confirmed that Ni greatly enhanced the interaction between NO and Mn sites, prompting the NH$_3$-SCR to follow the L-H mechanism more efficiently. In addition, Ni attenuated the strong surface Lewis acid of NiMnAlO$_x$ catalysts to medium surface Lewis acid and reduced the N$_2$O generated by the NH$_3$ over-oxidation pathway. The d-band PDOS analysis of Mn showed that the Jahn-Teller degradation promoted a more localized d-band and a greater degree of spin-polarization of Mn in NiMnAlO$_x$. The adsorption of paramagnetic NO on the NiMnAlO$_x$ catalyst was accompanied by a magnetic moment reversal in the active center and the catalyst as a whole, which weakened the large magnetic moment of the Mn site and led to the stabilization of the overall antiferromagnetic state of the catalyst. In contrast, the interaction of non-magnetic NH$_3$ with Mn sites did not undergo magnetic moment reversal and weakening of the magnetic moment of Mn sites, preventing the over-bonding of NH$_3$ with Mn. In addition, the PDOS of NO/NH$_3$ adsorption models of the catalysts provided insight into the mechanism and influence of the degradation of the Jahn-Teller effect and the reversal of magnetic moment reversal of Mn sites on the surface adsorption process.

CRediT authorship contribution statement

Qinghua Yan: Investigation, Writing – original draft. **Jiewen Xiao:** Visualization, Data curation, Validation, DFT calculations. **Rongrong Gui:** Visualization, Formal analysis. **Zhenyu Chen:** Supervision, Project administration. **Yuxin Wang:** Investigation, Software. **Yuran Li:** Validation, Supervision. **Tingyu Zhu:** Resources, Supervision, Project administration. **Qiang Wang:** Conceptualization, Writing – review & editing. **Yanjun Xin:** Resources, Writing – review & editing.
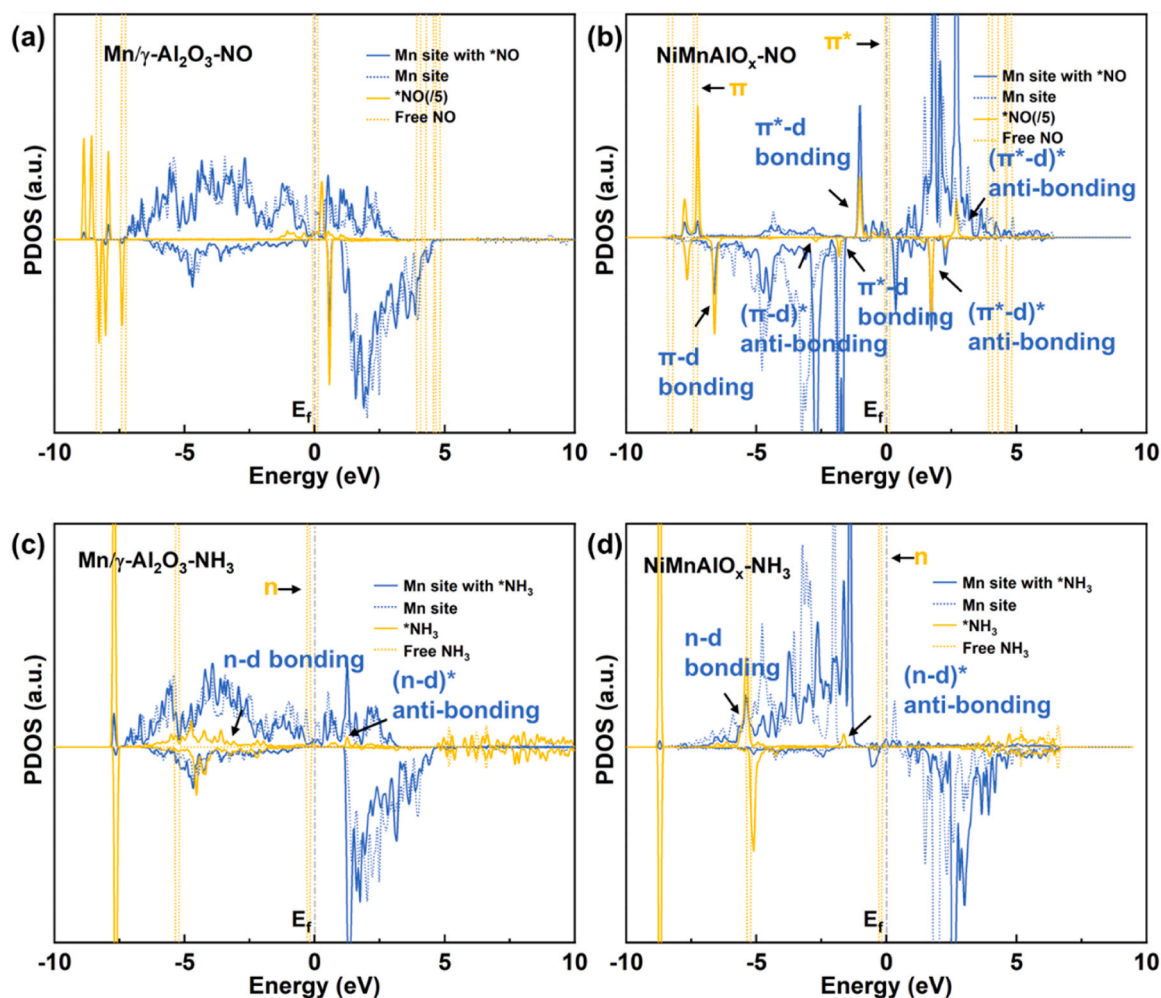
Fig. 11. PDOS profiles of NO and NH₃ adsorbed on (a, c) Mn/γ-Al₂O₃ and (b, d) NiMnAlOₓ. (Dash lines represents clean surfaces or small molecular and solid lines represents adsorbed small molecular or surfaces, grey dash dot lines mark Fermi level).

Declaration of Competing Interest

The authors declare that they have no known competing financial interests or personal relationships that could have appeared to influence the work reported in this paper.

Data availability

Data will be made available on request.

Appendix A. Supporting information

Supplementary data associated with this article can be found in the online version at doi:10.1016/j.apcatb.2023.123489.

References

[1] S.C. Anenberg, J. Miller, R. Minjares, L. Du, D.K. Henze, F. Lacey, C.S. Malley, L. Emberson, V. Franco, Z. Klimont, C. Heyes, Impacts and mitigation of excess diesel-related NOₓ emissions in 11 major vehicle markets, Nature 545 (2017) 467–471.

[2] A. Richter, J.P. Burrows, H. Nüß, C. Granier, U. Niemeier, Increase in tropospheric nitrogen dioxide over China observed from space, Nature 437 (2005) 129–132.

[3] L. Han, S. Cai, M. Gao, P. J.-y. Hasegawa, J. Wang, L. Zhang, D. Shi, Zhang, Selective catalytic reduction of NOₓ with NH₃ by using novel catalysts: state of the art and future prospects, Chem. Rev. 119 (2019) 10916–10976.

[4] Z. Zhang, R. Li, M. Wang, Y. Li, Y. Tong, P. Yang, Y. Zhu, Two steps synthesis of CeTiOₓ oxides nanotube catalyst: Enhanced activity, resistance of SO₂ and H₂O for low temperature NH₃-SCR of NOₓ, Appl. Catal. B: Environ. 282 (2021), 119542.

[5] H. Wang, Z. Qu, L. Liu, S. Dong, Y. Qiao, Promotion of NH₃-SCR activity by sulfate-modification over mesoporous Fe doped CeO₂ catalyst: Structure and mechanism, J. Hazard. Mater. 414 (2021), 125565.

[6] J. Fan, P. Ning, Z. Song, X. Liu, L. Wang, J. Wang, H. Wang, K. Long, Q. Zhang, Mechanistic aspects of NH₃-SCR reaction over CeO₂/TiO₂-ZrO₂-SO₄²⁻ catalyst: In situ DRIFTS investigation, Chem. Eng. J. 334 (2018) 855–863.

[7] B. Liu, J. Liu, L. Xin, T. Zhang, Y. Xu, F. Jiang, X. Liu, Unraveling reactivity descriptors and structure sensitivity in low-temperature NH₃-SCR reaction over CeTiOₓ catalysts: A combined computational and experimental study, ACS Catal. 11 (2021) 7613–7636.

[8] Q. Yan, Y. Gao, Y. Li, M.A. Vasiliades, S. Chen, C. Zhang, R. Gui, Q. Wang, T. Zhu, A.M. Efstathiou, Promotional effect of Ce doping in Cu₄Al₁Oₓ - LDO catalyst for low-T practical NH₃-SCR: Steady-state and transient kinetics studies, Appl. Catal. B: Environ. 255 (2019), 117749.

[9] Z. Chen, Q. Liu, L. Guo, S. Zhang, L. Pang, Y. Guo, T. Li, The promoting mechanism of in situ Zr doping on the hydrothermal stability of Fe-SSZ-13 catalyst for NH₃-SCR reaction, Appl. Catal. B: Environ. 286 (2021), 119816.

[10] W. Zhang, X. Shi, Z. Yan, Y. Shan, Y. Zhu, Y. Yu, H. He, Design of high-performance iron–niobium composite oxide catalysts for NH₃-SCR: Insights into the interaction between Fe and Nb, ACS Catal. 11 (2021) 9825–9836.

[11] X. Zhou, P. Wang, Z. Shen, S. Chen, Q. Wang, D. Cheng, D. Zhang, Low-temperature NO_x reduction over hydrothermally stable SCR catalysts by engineering low-coordinated Mn active sites, Chem. Eng. J. 442 (2018) 136182.

[12] X. Fang, Y. Liu, Y. Cheng, W. Cen, Mechanism of Ce-modified birnessite-MnO_2 in promoting SO_2 poisoning resistance for low-temperature NH_3-SCR, ACS Catal. 11 (2021) 4125–4135.

[13] Y. Chen, H. Yan, W. Teng, J. Li, W. Liu, S. Ren, J. Yang, Q. Liu, Comparative study on N_2O formation pathways over bulk MoO_3 and MoO_{3-x} nanosheets decorated Fe_2O_3-containing solid waste NH_3-SCR catalysts, Fuel 337 (2023), 127210.

[14] J. Yang, S. Ren, Y. zhou, Z. Su, L. Yao, J. Cao, L. Jiang, G. Hu, M. Kong, J. Yang, Q. Liu, In situ IR comparative study on N_2O formation pathways over different valence states manganese oxides catalysts during NH_3–SCR of NO, Chem. Eng. J. 397 (2020), 125446.

[15] F. Kapteijn, L. Singoredjo, A. Andreini, J.A. Moulijn, Activity and selectivity of pure manganese oxides in the selective catalytic reduction of nitric oxide with ammonia, Appl. Catal. B: Environ. 3 (1994) 173–189.

[16] Y. Niu, T. Shang, S. Hui, X. Zhang, Y. Lei, S. Lv, S. Wang, Synergistic removal of NO and N_2O in low-temperature SCR process with MnO_x/Ti based catalyst doped with Ce and V, Fuel 185 (2016) 316–322.

[17] Z. Chen, R. Guo, S. Ren, L. Chen, X. Li, M. Wang, Comparative analysis of the dual origins of the N_2O byproduct on MnO_x, FeO_x, and $MnFeO_x$ sphere catalysts for a low-temperature SCR of NO with NH_3, J. Mater. Chem. A 10 (2022) 21474–21491.

[18] L. Chen, S. Ren, Y. Jiang, L. Liu, M. Wang, J. Yang, Z. Chen, W. Liu, Q. Liu, Effect of Mn and Ce oxides on low-temperature NH_3-SCR performance over blast furnace slag-derived zeolite X supported catalysts, Fuel 320 (2022), 123969.

[19] L. Chen, S. Ren, X. Xing, J. Yang, J. Yang, M. Wang, Z. Chen, Q. Liu, Low-cost CuX catalyst from blast furnace slag waste for low-temperature NH_3-SCR: Nature of Cu active sites and influence of SO_2/H_2O, ACS Sustain. Chem. Eng. 10 (2022) 7739–7751.

[20] Z. Chen, S. Ren, M. Wang, J. Yang, L. Chen, W. Liu, Q. Liu, B. Su, Insights into samarium doping effects on catalytic activity and SO_2 tolerance of $MnFeO_x$ catalyst for low-temperature NH_3-SCR reaction, Fuel 321 (2022), 124113.

[21] L. Chen, R. Li, Z. Li, F. Yuan, X. Niu, Y. Zhu, Effect of Ni doping in $Ni_xMn_{1-x}Ti_{10}$ (x=0.1-0.5) on activity and SO_2 resistance for NH_3-SCR of NO studied with in situ DRIFTS, Catal. Sci. Technol. 7 (2017) 3243–3257.

[22] Y. Wan, W. Zhao, Y. Tang, L. Li, H. Wang, Y. Cui, J. Gu, Y. Li, J. Shi, Ni-Mn bi-metal oxide catalysts for the low temperature SCR removal of NO with NH_3, Appl. Catal. B: Environ. 148–149 (2014) 114–122.

[23] S. Deng, K. Zhuang, B. Xu, Y. Ding, L. Yu, Y. Fan, Promotional effect of iron oxide on the catalytic properties of Fe-MnO_x/TiO_2 (anatase) catalysts for the SCR reaction at low temperatures, Catal. Sci. Technol. 6 (2016) 1772–1778.

[24] P.G. Smirniotis, P.M. Sreekanth, D.A. Peña, R.G. Jenkins, Manganese oxide catalysts supported on TiO_2, Al_2O_3, and SiO_2: A comparison for low-temperature SCR of NO with NH_3, Ind. Eng. Chem. Res. 45 (2006) 6436–6443.

[25] W.S. Kijlstra, E.K. Poels, A. Bliek, B.M. Weckhuysen, R.A. Schoonheydt, Characterization of Al_2O_3-supported manganese oxides by electron spin resonance and diffuse reflectance spectroscopy, J. Phys. Chem. B 101 (1997) 309–316.

[26] Q. Wang, D. O'Hare, Recent advances in the synthesis and application of layered double hydroxide (LDH) nanosheets, Chem. Rev. 112 (2012) 4124–4155.

[27] J. Zhao, J. Chen, S. Xu, M. Shao, Q. Zhang, F. Wei, J. Ma, M. Wei, D.G. Evans, X. Duan, Hierarchical NiMn layered double hydroxide/carbon nanotubes architecture with superb energy density for flexible supercapacitors, Adv. Funct. Mater. 24 (2014) 2938–2946.

[28] R. Wang, Z. Qiu, S. Wan, Y. Wang, Q. Liu, J. Ding, Q. Zhong, Insight into mechanism of divalent metal cations with different d-bands classification in layered double hydroxides for light-driven CO_2 reduction, Chem. Eng. J. 427 (2022) 130863.

[29] N. Altaf, S. Liang, L. Huang, Q. Wang, Electro-derived Cu-Cu_2O nanocluster from LDH for stable and selective C_2 hydrocarbons production from CO_2 electrochemical reduction, J. Energy Chem. 48 (2020) 169–180.

[30] C. Xia, H. Huang, D. Liang, Y. Xie, F. Kong, Q. Yang, J. Fu, Z. Dou, Q. Zhang, Z. Meng, Adsorption of tetracycline hydrochloride on layered double hydroxide loaded carbon nanotubes and site energy distribution analysis, Chem. Eng. J. 443 (2022), 136398.

[31] J. Mittal, Recent progress in the synthesis of Layered Double Hydroxides and their application for the adsorptive removal of dyes: A review, J. Environ. Manag. 295 (2021) 113017.

[32] L. Gan, K. Li, W. Yang, J. Chen, Y. Peng, J. Li, Core-shell-like structured α-MnO_2@CeO_2 catalyst for selective catalytic reduction of NO: Promoted activity and SO_2 tolerance, Chem. Eng. J. 391 (2020) 123473.

[33] Y. Ren, Y. Yang, L. Chen, L. Wang, Y. Shi, P. Yin, W. Wang, M. Shao, X. Zhang, M. Wei, Synergetic effect of Cu^0-Cu^+ derived from layered double hydroxides toward catalytic transfer hydrogenation reaction, Appl. Catal. B: Environ. 314 (2022) 121515.

[34] P. Lu, Y. Liu, T. Zhou, Q. Wang, Y. Li, Recent advances in layered double hydroxides (LDHs) as two-dimensional membrane materials for gas and liquid separations, J. Membr. Sci. 567 (2018) 89–103.

[35] M. Bajdich, M. García-Mota, A. Vojvodic, J.K. Nørskov, A.T. Bell, Theoretical investigation of the activity of cobalt oxides for the electrochemical oxidation of water, J. Am. Chem. Soc. 135 (2013) 13521–13530.

[36] J.K. Nørskov, F. Studt, F. Abild-Pedersen, T. Bligaard. Fundamental Concepts in Heterogeneous Catalysis, first ed., John Wiley & Sons, 2014.

[37] R. Gui, X. Xiao, Y. Gao, Y. Li, T. Zhu, Q. Wang, Simultaneously achieving selective catalytic reduction of NO_x with NH_3 and catalytic oxidation of CO with O_2 over one finely optimized bifunctional catalyst $Mn_2Cu_1Al_1O_x$ at low temperatures, Appl. Catal. B: Environ. 306 (2022), 121104.

[38] P. Gholami, A. Khataee, M. Ritala, Template-free hierarchical trimetallic oxide photocatalyst derived from organically modified ZnCuCo layered double hydroxide, J. Clean. Prod. 366 (2022), 132761.

[39] B. Jiang, Y. Liu, Z. Wu, Low-temperature selective catalytic reduction of NO on MnO_x/TiO_2 prepared by different methods, J. Hazard. Mater. 162 (2009) 1249–1254.

[40] D. Liu, Q. He, S. Ding, L. Song, Structural regulation and support coupling effect of single-atom catalysts for heterogeneous catalysis, Adv. Energy Mater. 10 (2020) 2001482.

[41] B. Wang, M. Wang, L. Han, Y. Hou, W. Bao, C. Zhang, G. Feng, L. Chang, Z. Huang, J. Wang, Improved activity and SO_2 resistance by Sm-modulated redox of $MnCeSmTiO_x$ mesoporous amorphous oxides for low-temperature NH_3-SCR of NO, ACS Catal. 10 (2020) 9034–9045.

[42] H. Wang, W. Chen, W. Jin, Y. Liu, Mn mixed oxide catalysts supported on Sn-doped CoAl-LDO for low-temperature NH_3-SCR, Catal. Sci. Technol. 13 (2023) 3147–3157.

[43] F. Gao, X. Tang, Z. Sani, H. Yi, S. Zhao, Q. Yu, Y. Zhou, Y. Shi, S. Ni, Spinel-structured Mn–Ni nanosheets for NH_3-SCR of NO with good H_2O and SO_2 resistance at low temperature, Catal. Sci. Technol. 10 (2020) 7486–7501.

[44] N. Zhang, L. Li, Y. Guo, J. He, R. Wu, L. Song, G. Zhang, J. Zhao, D. Wang, H. He, A MnO_2-based catalyst with H_2O resistance for NH_3-SCR: Study of catalytic activity and reactants-H_2O competitive adsorption, Appl. Catal. B: Environ. 270 (2020), 118860.

[45] P. Wang, L. Yan, Y. Gu, S. Kuboon, H. Li, T. Yan, L. Shi, D. Zhang, Poisoning-resistant NO_x reduction in the presence of alkaline and heavy metals over H-SAPO-34-supported Ce-promoted Cu-based catalysts, Environ. Sci. Technol. 54 (2020) 6396–6405.

[46] J. Wang, Z. Yan, L. Liu, Y. Chen, Z. Zhang, X. Wang, In situ DRIFTS investigation on the SCR of NO with NH_3 over V_2O_5 catalyst supported by activated semi-coke, Appl. Surf. Sci. 313 (2014) 660–669.

[47] Q. Zhang, J. Fan, P. Ning, Z. Song, X. Liu, L. Wang, J. Wang, H. Wang, K. Long, In situ DRIFTS investigation of NH_3-SCR reaction over CeO_2/zirconium phosphate catalyst, Appl. Surf. Sci. 435 (2018) 1037–1045.

[48] H. Xue, X. Guo, T. Meng, D. Mao, Z. Ma, NH_3-SCR of NO over M/ZSM-5 (M = Mn, Co, Cu) catalysts: An in-situ DRIFTS study, Surf. Interfaces 29 (2022), 101722.

[49] Y. Liu, T. Gu, X. Weng, Y. Wang, Z. Wu, H. Wang, DRIFT studies on the selectivity promotion mechanism of Ca-modified Ce-Mn/TiO_2 catalysts for low-temperature NO reduction with NH_3, J. Phys. Chem. C. 116 (2012) 16582–16592.

[50] Z. Hu, X. Yong, D. Li, R.T. Yang, Synergism between palladium and nickel on Pd-Ni/TiO_2 for H_2-SCR: A transient DRIFTS study, J. Catal. 381 (2020) 204–214.

[51] K. Zha, C. Feng, L. Han, H. Li, T. Yan, S. Kuboon, L. Shi, D. Zhang, Promotional effects of Fe on manganese oxide octahedral molecular sieves for alkali-resistant catalytic reduction of NO_x: XAFS and in situ DRIFTs study, Chem. Eng. J. 381 (2020), 122764.

[52] Y. Jia, J. Jiang, R. Zheng, L. Guo, J. Yuan, S. Zhang, M. Gu, Insight into the reaction mechanism over PMoA for low temperature NH_3-SCR: A combined In-situ DRIFTs and DFT transition state calculations, J. Hazard. Mater. 412 (2021), 125258.

[53] I. Song, H. Lee, S.W. Jeon, D.H. Kim, Understanding the dynamic behavior of acid sites on TiO_2-supported vanadia catalysts via operando DRIFTS under SCR-relevant conditions, J. Catal. 382 (2020) 269–279.

[54] C. Chen, Y. Wang, J. Li, F. Tian, W. Chen, C. Feng, Y. Pan, Y. Liu, In situ construction of heteroatom F-doped Mn_3O_4 spinel catalysts with robust activity and SO_2 resistance for NH_3-SCR at low temperature, Appl. Catal. B: Environ. 338 (2023), 123086.

[55] S. Xie, L. Li, L. Jin, Y. Wu, H. Liu, Q. Qin, X. Wei, J. Liu, L. Dong, B. Li, Low temperature high activity of M (M = Ce, Fe, Co, Ni) doped M-Mn/TiO_2 catalysts for NH_3-SCR and in situ DRIFTS for investigating the reaction mechanism, Appl. Surf. Sci. 515 (2020), 146014.

[56] K. Alexopoulos, P. Hejduk, M. Witko, M.-F. Reyniers, G.B. Marin, Theoretical study of the effect of (001) TiO_2 anatase support on V_2O_5, J. Phys. Chem. C. 114 (2010) 3115–3130.

[57] S. Chen, M.A. Vasiliades, Q. Yan, G. Yang, X. Du, C. Zhang, Y. Li, T. Zhu, Q. Wang, A.M. Efstathiou, Remarkable N_2-selectivity enhancement of practical NH_3-SCR over $Co_{0.5}Mn_1Al_{0.75}O_x$-LDO: The role of Co investigated by transient kinetic and DFT mechanistic studies, Appl. Catal. B: Environ. 277 (2020) 119186.

[58] D.-B. Cao, X. Liu, J.P. Lewis, W. Guo, X. Wen, Tuning surface-electron spins on Fe_3O_4 (111) through chemisorption of carbon monoxide, Angew. Chem. Int. Edit. 134 (2022), e202202751.